

Leveraging the interplay between homogeneous and heterogeneous catalytic mechanisms: copper-iron nanoparticles working under chemically relevant tumor conditions

Javier Bonet-Aleta^{a,b,c}, Miguel Encinas^{a,b,c}, Esteban Urriolabeitia^d, Pilar Martin-Duque^{b,e,f,g}, Jose L. Hueso^{a,b,c}, Jesus Santamaria^{a,b,c,f}

^aInstitute of Nanoscience and Materials of Aragon (INMA), CSIC-Universidad de Zaragoza, Campus Río Ebro, Edificio I+D, C/ Poeta Mariano Esquillor, s/n, 50018, Zaragoza, Spain.

^bNetworking Research Center in Biomaterials, Bioengineering and Nanomedicine (CIBER-BBN), Madrid, Spain. Instituto de Salud Carlos III; 28029, Madrid, Spain.

^cDepartment of Chemical and Environmental Engineering; University of Zaragoza, Spain; Campus Rio Ebro, C/María de Luna, 3, 50018 Zaragoza, Spain.

^dInstituto de Síntesis Química y Catálisis Homogénea, ISQCH (CSIC-Universidad de Zaragoza), 50009 Zaragoza, Spain.

^eInstituto Aragonés de Ciencias de la Salud (IACS), Avenida San Juan Bosco, 13, 50009 Zaragoza, Spain.

^fInstituto de Investigación Sanitaria (IIS) Aragón, Avenida San Juan Bosco, 13, 50009 Zaragoza, Spain.

^gFundación Araid. Av. de Ranillas 1-D, 50018 Zaragoza, Spain.

ABSTRACT

The present work sheds light on a generally overlooked issue in the emerging field of bio-orthogonal catalysis within tumor microenvironments (TMEs): the interplay between homogeneous and heterogeneous catalytic processes. In most cases, previous works dealing with nanoparticle-based catalysis in the TME, focus on the effects obtained (e.g. tumor cell death) and attribute the results to heterogeneous processes alone. The specific mechanisms are rarely substantiated and, furthermore, the possibility of a significant contribution of homogeneous processes by leached species –and the complexes that they may form with biomolecules- is neither contemplated nor pursued. Herein, we have designed a bimetallic catalyst nanoparticle containing Cu and Fe species and we have been able to describe the whole picture in a more complex scenario where both homogeneous and heterogeneous processes are coupled and fostered under TME relevant chemical conditions. We investigate the preferential leaching of Cu ions in the presence of a TME overexpressed biomolecule such as glutathione (GSH). We demonstrate that these homogeneous processes initiated by the released by Cu-GSH interactions are in fact responsible for the greater part of the cell death effects found (GSH, a scavenger of reactive oxygen species is depleted and highly active superoxide anions are generated in the same catalytic cycle). The remaining solid CuFe nanoparticle becomes an active catalase-mimicking surrogate able to supply oxygen from oxygen reduced species, such as superoxide anions (by-product from GSH oxidation) and hydrogen peroxide, another species that is enriched in the TME. This enzyme-like activity is essential to sustain the homogeneous catalytic cycle in the oxygen-deprived tumor microenvironment. The combined heterogeneous-homogeneous mechanisms revealed themselves as highly efficient in selectively killing cancer cells, due to their higher GSH levels compared to healthy cell lines.

Glutathione (GSH) is a key peptide in the regulation of intracellular Reactive Oxygen Species (ROS) levels. Its role is of paramount importance in the tumor microenvironment (TME)¹, where GSH is overexpressed to counteract the overproduction of oxidizing species such as H₂O₂ that may disrupt redox homeostasis leading to apoptosis². GSH counteracts the generation of ROS via enzymatic reaction with the Glutathione Peroxidase (GPx) enzyme³. Consequently, GSH is quickly becoming the target of new cancer therapies¹. In addition, the high intratumoral GSH concentrations (up to mM^{4,5}) may interfere with emerging cancer therapies (Chemodynamic- (CDT), Sonodynamic- (SDT), and Photodynamic (PDT)) therapy that are ROS-dependent and become less effective in the presence of increased GSH levels⁶.

Nanocatalytic cancer therapy is rapidly emerging as a novel alternative able to trigger selective catalytic reactions in cancer cells to induce their apoptosis^{7,8}. Transition metal nanocatalysts in particular are able to promote GSH depletion via oxidation mechanisms thereby interfering in the survival and protection mechanisms of cancer cells⁷. The ideal scenario involves catalytic materials that can eliminate antioxidant molecules such as GSH, while simultaneously promoting the generation of ROS. It is obvious that a deeper understanding of the role of nanocatalysts in the TME is critical to enhance their efficient action. However, this still represents a formidable challenge: the catalytic mechanisms of the most promising nanoplateforms and their interplay with key biomolecules remains elusive due to the complexity of the interactions in the TME.

A fundamental aspect of the interaction between catalyst nanoparticles and the TME that is often overlooked relates to the surface phenomena involved. In particular, leaching (i.e. metal ions lixiviated from the surface of the nanostructured catalyts into the surrounding fluid) is a phenomenon likely to have a strong influence on the final therapy outcome. Previous investigations have aimed at designing nanoplateforms with pH-triggered metal ion lixiviation given the mildly-acidic TME⁹. The influence of acidity in metal lixiviation has been explored in several cancer-related works for Fe^{10,11}, Mn¹²⁻¹⁴ or Cu¹⁵⁻²⁰. It has also been shown that the complex chemical composition in biological environments includes molecular species such as aminoacids, that may promote lixiviation especially in the case of Cu²¹⁻²³. However, the role that these species may play as catalyts and the interactions with heterogeneous processes fostered by the solid phase have not been investigated.

Some valuable insights can be derived from conventional, aqueous phase catalysis. Eremin et al. ²⁴ recently pictured an expanded vision of the nature of transition-metal-catalyzed reactions. These authors described the well-established scenarios of (i) Molecular-based Catalysis and (ii) Nanoparticle-based Catalysis (heterogeneous catalysis) and presented a perspective of three additional intermediate scenarios given by (iii) Lixiviation-driven catalysis; (iv) "Cocktail" of catalyts derived from the nanoparticle (clusters, atoms, lixiviated ions) and (v) Dynamic catalytic systems. The

action of the catalyst nanoparticles used in medical applications is generally interpreted on the premises of purely heterogeneous mechanisms. Only in a few cases, (e.g. MnO₂-based nanomaterials, where dissolution of the nano-oxide structure through reaction with GSH is followed by Fenton processes facilitated by the as-formed Mn²⁺ ions) an attempt has been made to describe processes closer to lixiviation-driven catalysis. It must be noticed that the nanoplatforms evaluated as catalysts for cancer therapy are usually composed by more than one metal, (e.g. Cu₂MoS₄²⁵, MnFe₂O₄²⁶, CuFe₂O₄²⁷, Copper/Manganese silicate¹⁷, Cu_xFe_yS_z²⁸ or SrCuSi₄O₁₀²⁰) and these may be affected to a different extent by lixiviation phenomena under the mildly-acidic, hypoxic and GSH-enriched conditions prevalent in the TME. In any case, issues such as the extent of the lixiviation process, the possibility of a preferential leaching of a specific transition metal or the influence of specific chemical species present in the TME remain mostly unexplored. At present, is not possible to state whether the therapeutic action of nanocatalysts in the TME is attributable to lixiviated ions, a purely heterogeneous reaction, or a combination of both phenomena.

Here, we have thoroughly evaluated the catalytic mechanisms behind the action of a copper-iron mixed oxide (CuFe) nanocatalyst under representative conditions for a TME. This is a bimetallic system, complex enough to illustrate the main phenomena taking place. Our results shed light on the interplay between heterogeneous and homogeneous processes occurring in the presence of GSH. We report for the first time how the presence of elevated levels of GSH induces a preferential lixiviation of Cu species, initiating a homogeneous catalytic cycle that efficiently oxidizes GSH into Glutathione Disulfide (GSSG), assisted by the *in situ* formation of Cu-GSH coordination complexes. Simultaneously, the progressively Fe-enriched NP gives rise to heterogeneous catalytic cycles using ROS generated in the homogeneous GSH oxidation cycle (**Fig. 1**) or the overexpressed H₂O₂ present in the tumoral media^{29,30}. The system chosen is of especial interest, considering the increasing relevance of Cu and its interaction with key processes in cancer development³¹. Overall, the results presented in this work provide new insight on the dynamics of the chemical reactions inside the TME and valuable clues for the design of more efficient catalysts to operate in this environment.

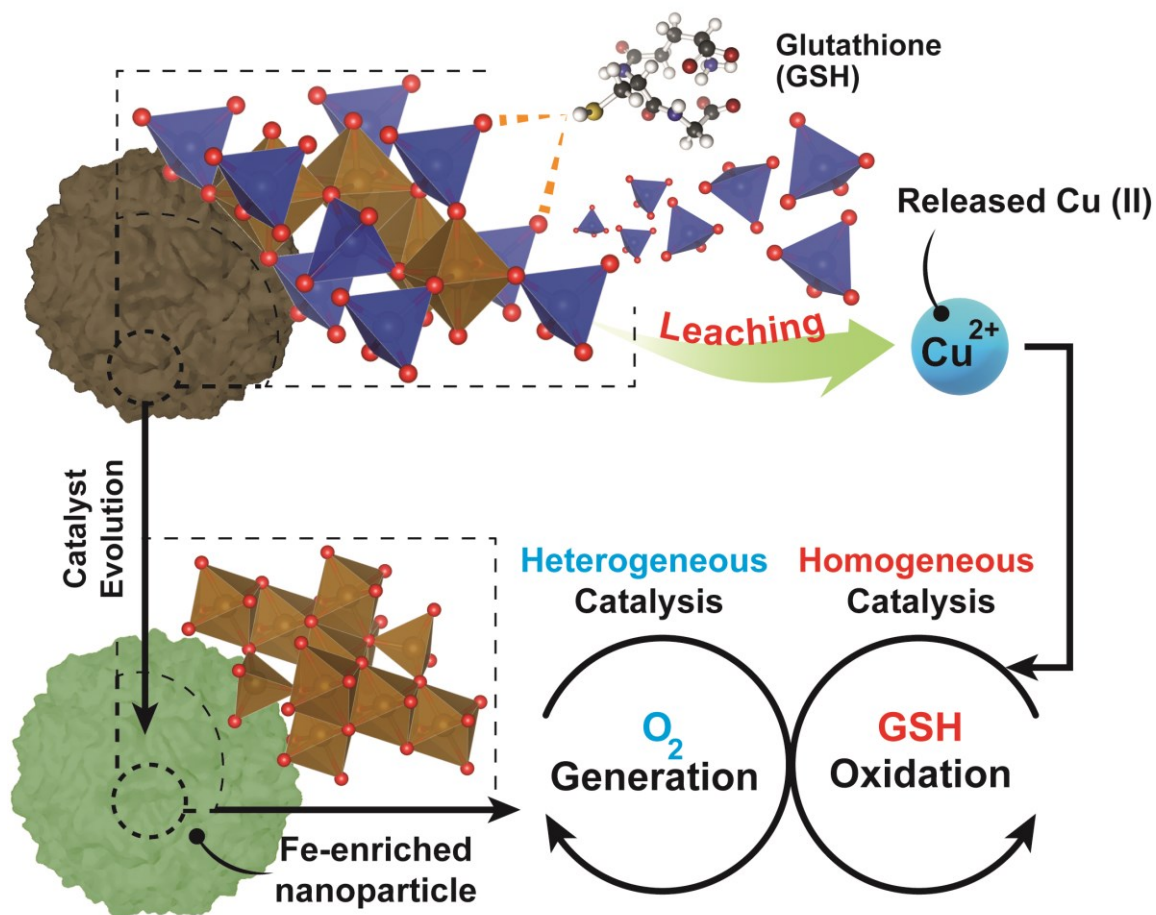


Fig. 1. Simplified overview of the homogeneous-heterogeneous processes fostered by the CuFe nanocatalyst in the presence of GSH. After a GSH-triggered Cu release from the nanocatalyst, Cu^{2+} catalyze the homogeneous oxidation of GSH into GSSG. Simultaneously, Fe(III) species present on the nanoparticle surface catalyze the conversion of H_2O_2 and $\cdot\text{O}_2^-$ species, considered as by-products from GSH oxidation into O_2 necessary to sustain the GSH depletion homogeneous cycle.

RESULTS

Cation leaching in the presence of GSH. The influence of GSH on the release of ionic Cu and Fe from the CuFe_2O_4 nanocatalyst was quantified by Microwave Plasma -Atomic Emission Spectroscopy (see Experimental section for details). The presence of GSH at a concentration of 5 mM changed considerably the leaching patterns. Thus, the release of Cu was strongly enhanced, with a cumulative release of ca. 70% of the initial Cu in the particle after 24 h (compared to about 20% in the absence of GSH). On the other hand, while Fe is not expected to be lixiviated significantly at this pH, we found that ca. 30% of the initial Fe content was released from the nanoparticle after 24 h (see **Fig. 2a**). We attribute this behavior to the generation of high-energy vacancies after GSH-triggered Cu release that facilitates the transfer of Fe into the solution³². The fact that Cu release is favored in the presence of GSH can be anticipated since previous works had reported Cu lixiviation from CuO nanoparticles in the presence of aminoacids or peptides^{21,22}. Interestingly, at lower pH values (pH of 5.80, close to the pH in a solid tumor medium) the extent of leaching for both Cu and Fe in the presence of GSH was reduced (**Fig. 2-b**), although the percentage of Cu leached doubles that of iron. Considering the different ionic forms of GSH upon varying the pH³³ (**Fig. 2-c**), this behavior can be linked to the stronger nucleophilic character of -SH group from GSH species as pH increases³⁴. Compared to -SH, thiolate ($-\text{S}^-$) form exhibits much stronger nucleophile behavior and the processes where $-\text{S}^-$ is involved may occur even at pH values far below thiol pK_a ³⁵, which may explain the promotion of Cu leaching at higher pH.

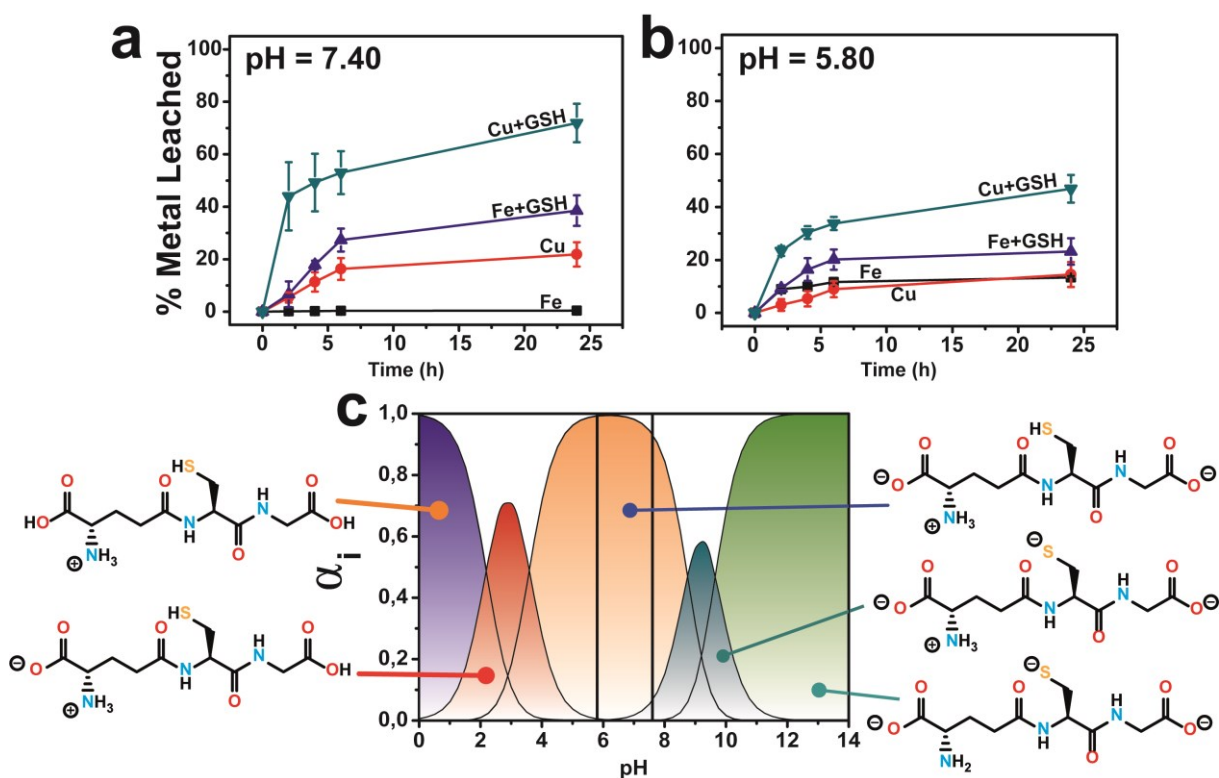


Fig. 2. GSH effect on the evolution of copper and iron cations lixiviated at different pH media: (a) pH = 7.4; (b) pH = 5.80; (c) Different GSH ionic species as a function of different pH values; Vertical lines represent the pH of selected experimental conditions for a better identification of expected GSH species; GSH concentration was set to 5 mM. Speciation diagram was generated using pK_a values obtained from [36].

Homogeneous GSH oxidation by cations leached from CuFe nanoparticles. After the abrupt cation release observed in the presence of GSH (Fig 2. a-b) and its preferential action towards the lixiviation of Cu (roughly twice as much Cu is released, compared to Fe), it is reasonable to assume a catalytic scenario mainly composed by aqueous Cu^{2+} ions and GSH (5 mM). This is relevant because previous works have described a evolution of GSH into its oxidized form (GSSG) catalyzed by Cu^{2+} [37]. In this scenario, O_2 could act as electron acceptor yielding reduced reactive oxygen species ($\bullet O_2$ [38,39] and H_2O_2 [37]) and GSSG as products, respectively (see Fig. 3a). Encouraged by these perspectives, we have explored the possibility of fostering homogeneous oxidation processes using the cations released from our $CuFe_2O_4$ nanocatalyst, while retaining the heterogeneous catalytic activity of the nanoparticles themselves.

In order to analyze the potential contribution of each lixiviated metal (Fe, Cu) in the homogeneous catalysis of GSH we performed a series of control experiments using chloride salt precursors ($CuCl_2$ and $FeCl_3$, respectively). We carried out 1H -Nuclear Magnetic Resonance (1H -NMR) analysis of the mixture $CuCl_2+GSH$ (Fig. 3b) to characterize the $Cu(SG)_2$ complex [39-43]. These assays were

performed in the absence of O₂ to prevent the total evolution of the reaction to products. The resulting spectra revealed a splitting of the β-CH₂ protons of the Cys residue of GSH, appearing as an unresolved multiplet at 2.86 ppm into a well defined AB spin system at 3.22 and 2.88 ppm, due to the bonding of the S atom to the reduced Cu(I) center^{39,44}. Other signals remained almost unchanged, suggesting that only the S atom is involved in bonding of GSH to Cu(I). This is in accordance with Hard Soft Acid Base theory (HSAB), soft-basic thiol (-SH) groups from GSH tend to bond soft-acidic Cu(I) centers⁴⁵.

Diffusion-ordered NMR spectroscopy (DOSY) experiments were also performed with GSH, GSSG and the CuCl₂+GSH binary mixture to determine the molecular size of each molecule and complex intermediates present in the solution based on their diffusion coefficients (D, m²·s⁻¹). The diffusion coefficients from the control experiments with GSH and GSSG (**Fig. S1a-b**) were adjusted to 3.98·10⁻¹⁰ and 2.75·10⁻¹⁰ m²·s⁻¹, respectively. Likewise, their corresponding hydrodynamic radii calculated through Stokes-Einstein equation were 0.6 and 0.9 nm. These values are in good agreement with intramolecular distances obtained in X-ray structures for GSH⁴⁶⁻⁴⁸ and GSSG^{49,50}. DOSY analysis of the CuCl₂+GSH binary mixture yielded a product with a D = 2.75·10⁻¹⁰ m²·s⁻¹ (**Fig. 32a**). In the presence of Cu²⁺, the species formed are larger than GSH (**Fig. S1a**) but of a similar size in comparison with GSSG (**Fig. S1b**). The complex Cu(SG)₂ is formed under these conditions³⁹⁻⁴³, which exhibit a rather analogous coefficient D with respect to GSSG. Also, we were able to confirm the formation of the Cu complex through the homogeneous catalytic cycle of figure 3a using High Resolution Mass Spectroscopy-ElectroSpray Ionization (HRMS-ESI) (**Fig. 3c**), that allowed identification of peaks corresponding to [GSSG+H]⁺ (m/z = 613.1613) and [Cu(SG)₂+H]⁺ (m/z = 675.0801). Ngamchuea et al.³⁷ studied the Cu(II)-mediated GSH catalytic oxidation and suggested a reaction pathway based on kinetic experiments where Cu(SG)₂, the same species detected in our control experiments (**Fig. 3-c**) also acted as reaction intermediate.

We also evaluated the potential contribution of Fe species to form complexes with GSH. In this case, control experiments with FeCl₃ were carried out at pH = 3.60 to minimize the formation of iron hydroxide species which interfere with NMR measurements and the introduction of species that are not normally present at physiological pH. ¹H-NMR and DOSY control experiments with FeCl₃ confirmed the formation of [Fe-(SG)_x] complexes (**Fig. S3a-b**), with proton chemical shifts at 3.04 and 2.76 ppm corresponding to assignments previously reported in the literature^{51,52}. In addition, HRMS-ESI analysis revealed the formation of [Fe₂(SG)₂+H]⁺ (m/z = 725.0352) and [Fe(SG)+H]⁺ (m/z = 363.0173) complexes (**Fig. S4**)⁵¹.

Once the formation of complexes with Cu and Fe cations were confirmed, analogous experiments with the CuFe nanocatalyst were subsequently carried out in the presence of GSH. The Cu lixiviated at pH = 7.4 interacted with the excess of GSH like in the control experiments. ¹H-NMR and DOSY

analysis of the solution (**Fig. 3b and Fig. S2b**), revealed both the presence of unreacted GSH ($D=4 \cdot 10^{-10} \text{ m}^2 \cdot \text{s}^{-1}$) and the formation of species with $D = 2.70 \cdot 10^{-10} \text{ m}^2 \cdot \text{s}^{-1}$. Taking into account the control experiments with CuCl_2 , the formation of the $\text{Cu}(\text{SG})_2$ intermediates seems also very likely in the presence of the CuFe catalyst. The widening on the spectra signals can be attributed to different equilibria established between GSH and $\text{Cu}(\text{SG})_2$ ^{42,53}. The presence of very small amounts of paramagnetic $[\text{Fe}-(\text{SG})_x]$ complexes cannot be discarded, and could also contribute to the widened signal. MS-ESI analysis of the solution at different reaction times (3-24h) yielded a mixture of Cu-SG-derived fragments (**Fig. S5**) supporting the hypothesis of Cu-SG as reaction intermediate in the catalytic cycle.

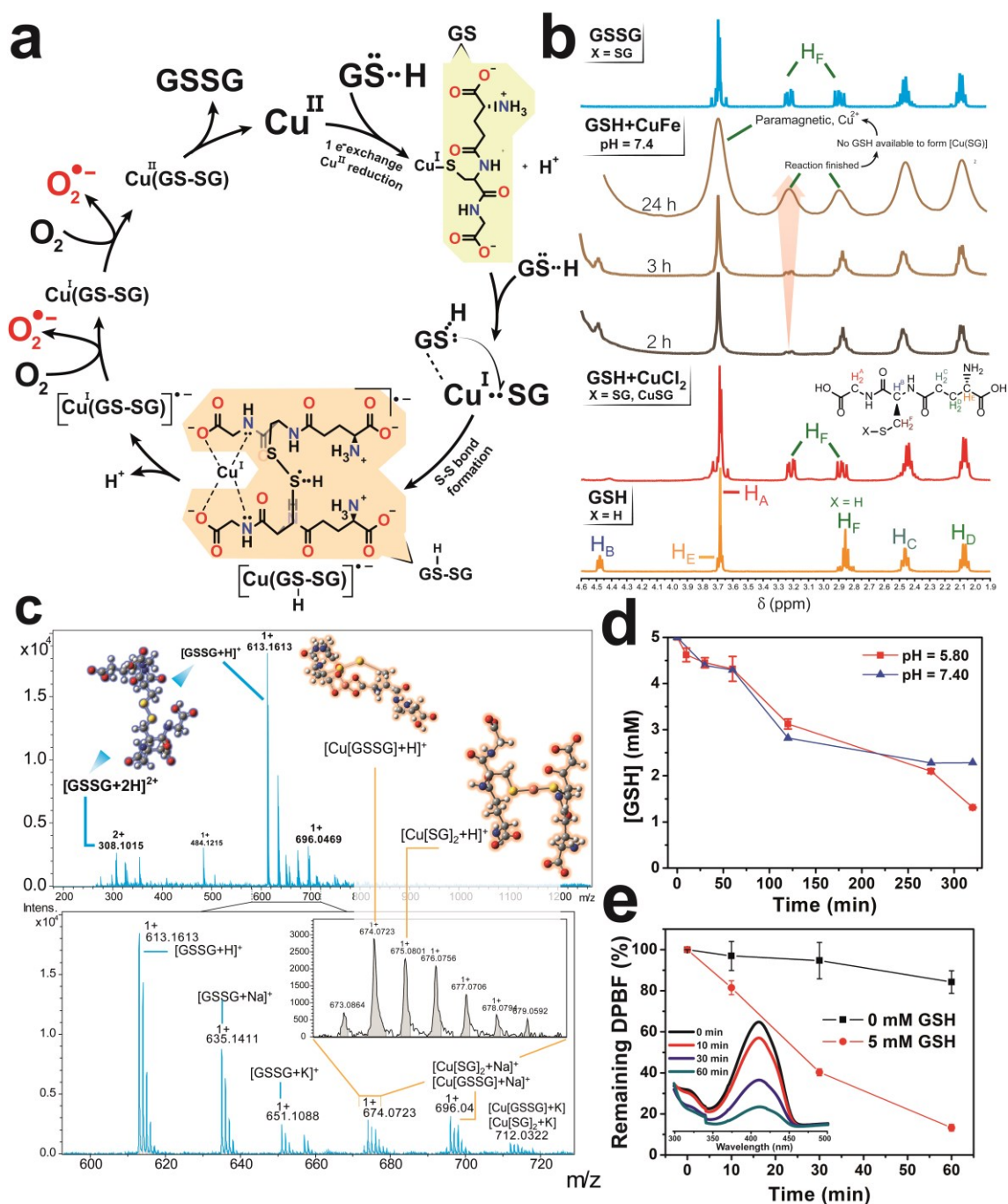


Fig. 3. Homogeneous catalysis of ionic Cu and GSH with O₂. (a) Proposed homogeneous catalytic cycle for the Cu-assisted GSH oxidation. The reoxidation of Cu(SG)₂ to Cu(GSSG) involves a reaction between the Cu(GS-SG)^{•-} complex and O₂, yielding superoxide radical species ([•]O₂⁻) as reaction by-product. The shaded areas correspond to the structure of GS and GS(H)SG, which are abbreviated for a better understanding; (b) ¹H NMR spectra of GSH, GSSG, GSH+CuCl₂ and GSH+CuFe at different reaction times (2, 3 and 24 h) with the corresponding proton assignments. ¹H NMR signal at 3.22 ppm implies a chemical modification near -SH group of the native GSH molecule, either [Cu(SG)₂]⁺ or GSSG formation. ¹H NMR reaction spectra at 24h is clearly altered due to paramagnetism induced by free Cu²⁺ in solution, since the reaction is complete and no GSH is

available to coordinate Cu^{2+} ; (c) HRMS-ESI from control experiments with CuCl_2 +GSH binary mixture in anaerobic conditions to quench the catalytic reaction. Two peaks at $m/z = 613.16$ and 635.14 corresponding to $[\text{GSSG-H}]^+$ and $[\text{GSSG+Na}]^+$ confirmed the generation of GSH oxidation product. The catalytic intermediate $\text{Cu}(\text{SG})_2$ is detected at $m/z = 674$ and 675 , respectively; (d) Evolution of GSH concentration in the presence of the CuFe nanocatalyst at pH 7.40 or 5.80 (adjusted with HCO_3^-), 37°C , $[\text{GSH}]_0 = 5\text{ mM}$; $[\text{CuFe}] = 0.1\text{ mg}\cdot\text{mL}^{-1}$; (e) Influence of GSH on the generation of anion superoxide species $\cdot\text{O}_2^-$ as side-product of the Cu-catalyzed GSH oxidation. The absorbance of DPBF at a wavelength of 411 nm is used as indirect probe; Reaction conditions: pH = 7.40 (adjusted with HCO_3^-), $[\text{GSH}]_0 = 5\text{ mM}$, $[\text{DPBF}]_0 = 0.1\text{ mM}$, $[\text{CuFe}] = 0.1\text{ mg}\cdot\text{mL}^{-1}$.

GSH levels were monitored via Ultra Performance Liquid Chromatography-Photo Diode Array (UPLC-PDA) and revealed an important decrease at pH=7.40 and 5.80 due to the catalytic activity of the Cu lixiviated by GSH (**Fig. 4d**). Remarkably, the presence of superoxide anion $\cdot\text{O}_2^-$ was also detected in the presence of GSH (**Fig. 3e**) using 1,3-Diphenylisobenzofuran (DPBF) as analytical probe (see **Fig. S6**). This allows us to propose a homogeneous catalytic reaction taking place mainly between the Cu^{2+} cations released from the CuFe catalyst and GSH (reaction step displayed in **Fig. 3a**): (i) GSH is able to bind and reduce aqueous Cu^{2+} species into Cu^+ through -SH group to form the $\text{Cu}^{\text{I}}(\text{SG})$ intermediate; (ii) A second GSH molecule is able to cleave the Cu-S bond to promote S-S formation through a radical process³⁵. This step is thermodynamically favored since S-S bond energy is larger in comparison to Cu-S (429 vs 285 kJ/mol, respectively⁵⁴). Following reported thiol oxidation kinetics³⁵, we propose the (iii) formation of the radical intermediate $[\text{Cu}^{\text{I}}(\text{GSSG})]^\cdot-$. O_2 acting as electron acceptor withdraws an electron from this disulfide radical anion (**Fig. S7**) (iv) to yield the superoxide anion $\cdot\text{O}_2^-$ that we have been able to detect together with $\text{Cu}^{\text{I}}(\text{GSSG})$. After this fast electron transfer, (v) the Cu^{I} center rapidly oxidizes into Cu^{II} in the presence of O_2 ⁴². (vi) The catalytic cycle is restored after GSSG is detached from the coordination sphere of Cu^{II} and replaced by a fresh GSH molecule. In the presence of a GSH excess, the $\text{Cu}^{\text{II}}(\text{GSSG})$ complex exchanges GSSG by GSH to restart the catalytic cycle⁴². This process is also thermodynamically favored, since the formation constant ($\log K'$) of $\text{Cu}(\text{SG})_2$ is significantly higher (26.6)⁵⁵ than $\text{Cu}(\text{GSSG})$ (3.63)⁵⁶. The appearance of the $\text{Cu}(\text{SG})_2$ complex is also favored by pH values typically met in a tumor microenvironment (**Fig S8-S9**). Although the lixiviation of Cu triggered by GSH proceeds at a slower pace at pH = 5.80 (see **Fig. 2b**), the percentage of Cu leached after 2 h of reaction reached ~25%, enough to produce the oxidation of roughly half of the initial GSH at that time (**Fig. 3d**).

The experiments with the CuFe NPs and GSH were also performed under acidic conditions. After 3 hours of reaction, $^1\text{H-NMR}$ analysis (**Fig. S3a**) showed no meaningful fractions of $\text{GSSG}/\text{Fe}(\text{SG})$ complex formed. UPLC-PDA and MS-ESI analyses further corroborated the lower conversion of GSH in the presence of lixiviated Fe ions (**Fig. S10** and **Fig. S11**, respectively). While an increase of the $[\text{Fe}(\text{SG})+\text{H}]^+$ signal was found after 24 h of reaction (**Fig. S8a**), a significant concentration of GSH

was still present (**Fig. S8b**). These GSH-oxidation results together with previous MP-AES results at neutral pH (**Fig. 2a**) further suggest a limited influence of Fe in the homogeneous conversion of GSH. Two factors are key to justify these phenomena: (i) the much larger standard reduction potential of $\text{Fe}^{3+/2+}$ ($E^0=+0.77$ V compared to $+0.153$ V for $\text{Cu}^{2+/+}$) implies a comparatively slower catalytic cycle since the regeneration of Fe^{3+} species to restart the cycle requires a higher energy demand, an energy penalty analogous to that observed in Fenton-like processes⁵⁷. (ii) The scarcity of labile Fe^{3+} available, both due to its slower leaching rate compared to Cu (**Fig. 2a**) and to the fact that at physiological pH released iron tend to rapidly form $\text{Fe}(\text{OH})_3$ species⁵⁸.

Heterogeneous catalase-mimicking response of the Fe-enriched solid nanoparticles. Given the strong Cu release in comparison with the much less intense Fe lixiviation, we investigated the morphological and catalytic properties of the progressively Fe-enriched nanoparticles. After the interaction with GSH, most of Cu present in the nanoparticle is lixiviated to the aqueous media (see **Fig. 2a**). This was confirmed by High-Angle Annular Dark Field-Scanning Transmission Electron Microscopy (HAADF-STEM) and Energy Dispersive X-ray spectroscopy (EDX) mapping analysis of the nanoparticle before (**Fig. 4a**) and after (**Fig. 4-b**) reaction, revealing a very significant Fe enrichment following the preferential leaching of Cu after its interaction with GSH. X-ray Photoelectron Spectroscopy (XPS) analysis of the CuFe nanocatalyst further confirms the strong reduction of the atomic percentage of copper at the surface in comparison with the original sample (0.28 atomic %Cu after exposure, compared to 7.80 before, a 28-fold decrease, see **Table S1-2**). This is further supported by the significant reduction of the $\text{Cu}2p_{3/2}$ photoemission contribution after incubation with GSH (**Fig. 4c**). In addition, the oxidation state of Cu is strongly affected by the process. The reduced Cu content is now enriched in Cu^+ as shown by the ratios of the contributions at 932.6 and 934.3 eV due to the reduction capability of GSH⁵⁹, compared to the original sample with a higher ratio of Cu(II) to Cu(I) states⁶⁰. In contrast, the Fe surface atomic percentage slightly increases (see **Table S1-2**) as Cu species on the surface are removed. TEM analysis of the CuFe nanocatalyst after one hour of incubation with different GSH concentrations reveals that a certain reduction of nanoparticle size takes place in the presence of high GSH concentrations (i.e. 5 mM) as a consequence of metal leaching (**Fig. 4d**). XRD analysis showed an important decrease of the intensity corresponding to the (400) diffraction peak⁶¹ which accounts for the crystalline plane that includes four tetrahedral Cu sites (**Fig. S12a-b**). This reduction is also consistent with the selective loss of copper sites upon the incubation with GSH (**Fig. S13a**). In contrast, the Fe-enriched remaining solid nanoparticle matches well with the XRD patterns of Fe_3O_4 and CuFe_2O_4 (**Fig. S12a**).

Fe-based oxides have been reported as active catalysts to transform ROS species, such as $\bullet\text{O}_2^{-62,63}$ or $\text{H}_2\text{O}_2^{7,27,64}$ into H_2O_2 and O_2 , respectively. Specifically, both species ($\bullet\text{O}_2^-$ and H_2O_2) are interesting in our system. $\bullet\text{O}_2^-$ is a reaction side-product resulting from the homogeneous catalytic cycle (**Fig. 3b**) and H_2O_2 is both an intratumoral overexpressed molecule^{29,65} and a reported by-product of Cu-

catalyzed GSH oxidation in the homogeneous phase³⁷. Thus, the Fe-enriched fraction of our catalyst is not a mere spectator of the homogeneous catalytic cycle. On the contrary, it becomes an active agent in generating oxygen from H₂O₂ under the hypoxic conditions (i.e. low O₂ concentration) prevailing in TME (**Fig. 4-e**). This is clearly shown in where after each H₂O₂ injection a clear increase in the concentration of dissolved oxygen can be observed in the presence of the Fe-enriched catalyst (**Fig. 4f**), acting as a catalase-mimicking surrogate. This is in contrast with the results obtained when the same experiment was repeated in the presence of the Cu leachate from the catalyst, where no oxygen generation could be observed. The generated oxygen allows to complete and sustain the homogeneous GSH-oxidation cycle, which needs O₂ as final electron acceptor⁶⁶. Interestingly, while the Fe-enriched solid nanocatalyst was able to decompose H₂O₂ into O₂ (**Fig. 4f**), it showed negligible activity towards •OH production through Fenton-like reaction (**Fig. S13**).

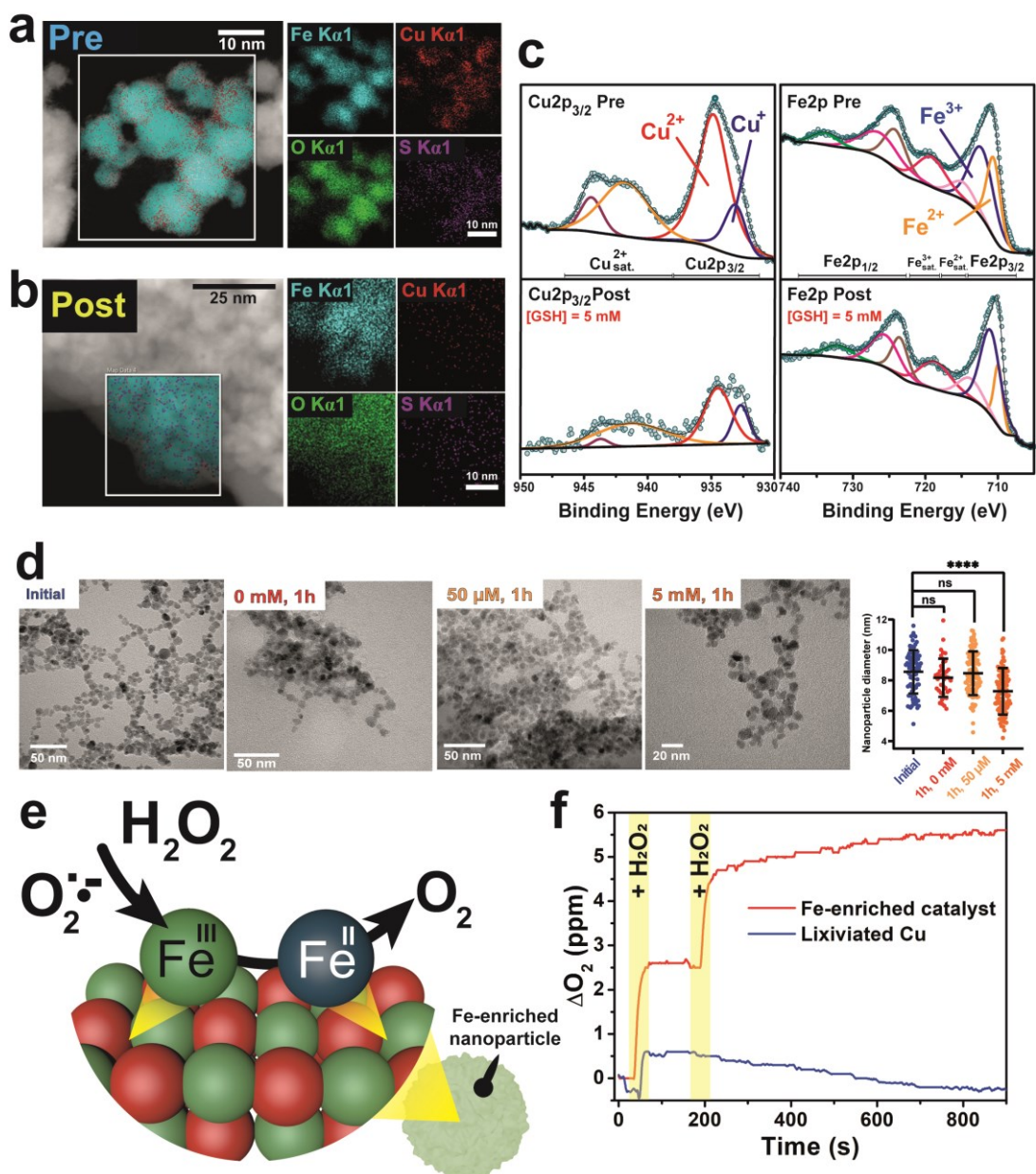


Fig. 4. Heterogeneous catalysis on the Fe-enriched nanoparticle surface: (a-b) STEM-EDX images before/after catalyst interaction with GSH. Prior to the GSH-triggered lixiviation of Cu, Fe and Cu co-localize within the crystalline network of the nanoparticle oxide. However, after GSH exposition, Cu starts to be released and its presence in the nanoparticle is strongly reduced; (c) X-ray photoemission spectra corresponding to the Cu2p_{3/2} and Fe 2p regions before and after reaction of the CuFe nanocatalyst with GSH; As a consequence of leaching process, the intensity of Cu signal is close to noise; (d) TEM images of the CuFe nanocatalyst after 1 hour incubation with different GSH concentrations of relevant at the intracellular and extracellular levels. Size analysis of individual nanoparticles reveals a certain reduction of size in the presence of large concentrations (5 mM) of GSH; (f) Catalytic O₂ generation from reduced oxygen species resultant from GSH oxidation (mainly \bullet O₂⁻ and H₂O₂) assisted by the resultant Fe-enriched nanoparticle after Cu leaching (g) O₂ generation

capabilities of the Fe-enriched nanoparticles and of the supernatant containing leached Cu cations at pH = 7.40; $[H_2O_2]_0 = 1 \text{ mM}$, $[CuFe] = 0.1 \text{ mg}\cdot\text{mL}^{-1}$; Addition of H_2O_2 is highlighted.

Interplay of homogeneous and heterogeneous catalysis in healthy and cancer cells with different GSH levels. To evaluate the biological action of the CuFe nanocatalyst additional experiments were carried out against different cell lines. Several tumor cell lines were specifically selected for their intrinsic high GSH levels, while healthy cell lines (i.e. fibroblasts and mesenchymal cells) with lower GSH concentrations were used as control^{67,68}. Specifically, four different tumor cell lines were chosen in order to assess the cytotoxic effect of this nanocatalyst: U251-MG and U87-MG (both malignant glioblastoma cell lines), SKOV-3 (ovarian cancer cell line) and HeLa (cervical cancer cell line). The aim of the study was to compare the behavior of cell lines against the action of our nanocatalyst, since it is expected to have a variable effect depending on the specific GSH content.

The results of the cytotoxicity studies after different times of incubation with the CuFe nanocatalyst (**Fig. 5a**) revealed a clear effect: the viability of the four tumor cell lines was reduced, even at low concentrations of the catalyst and reduced incubation times (see **Fig. 5a**). In contrast, the non-tumoral cell lines remained viable in the presence of much higher concentrations of the catalyst. The microscopy study is consistent with the cytotoxicity results, showing a marked impairment of morphology for the tumoral cell lines exposed to the CuFe catalyst (**Fig. 5b**).

Up to now, the interaction between Cu and Fe based nanoparticles and GSH has been either interpreted from the perspective of a heterogeneous process taking place at the nanoparticle-liquid interface or directly neglected. We have detected $\bullet O_2^-$ as the reaction by-product of Cu-catalyzed GSH oxidation (although H_2O_2 is also reported³⁷), a reaction taking place homogeneously with leached Cu species, i.e. while GSH interacts with the surface to produce the release of Cu(I) species, the GSH oxidation itself would be a homogeneous process taking place in the bulk of the solution and not on the catalyst particle. However, both reaction byproducts $\bullet O_2^-$ and H_2O_2 are capable of interacting with the remaining Fe-enriched nanoparticle which acts as an heterogeneous catalyst yielding O_2 , which in turn is necessary to sustain the homogeneous GSH oxidation.

Taking into account the above results, we propose the following reaction mechanism (see **Fig. 6**): (i) In a first step, nucleophilic thiol (-SH) groups from GSH promote the release of Cu species from the nanocatalyst crystalline network. GSH overexpressed in TME forms a coordination complex with released Cu, $(Cu(SG)_2)$. The formation of this complex effectively removes free Cu(I) species from the environment, shifting liquid phase equilibria and increasing the rate of Cu leaching; (ii) The $Cu(SG)_2$ complex starts a homogeneous catalytic cycle where GSH is finally oxidized to GSSG by dissolved O_2 ; This latter process entails an electron transfer from $[Cu^I(GSSG)]^-$ to O_2 , promoting the generation of $\bullet O_2^-$ radicals which readily (iii) react with the Fe^{III} sites remaining in the solid nanocatalyst through a

Haber-Weiss reaction^{69,70} to regenerate O_2 that feeds the homogeneously Cu-catalyzed reaction. Moreover, additional O_2 is produced by the Fe-enriched catalytic nanoparticle using environmental H_2O_2 (**Figure 4f**). Finally, (iv) GSSG is released from the coordination sphere of Cu^{2+} , which becomes available to be reduced by GSH and re-start the catalytic cycle. The proposed mechanism constitutes a perfect example of how two catalytic processes, namely the homogeneous Cu-catalyzed GSH oxidation and the heterogeneously catalyzed processes of H_2O_2 decomposition and $\bullet O_2$ reaction are synergistically coupled to provide the efficient oxidation of a key tumor metabolite (GSH) allowing to circumvent O_2 -scarcity in tumor microenvironment.

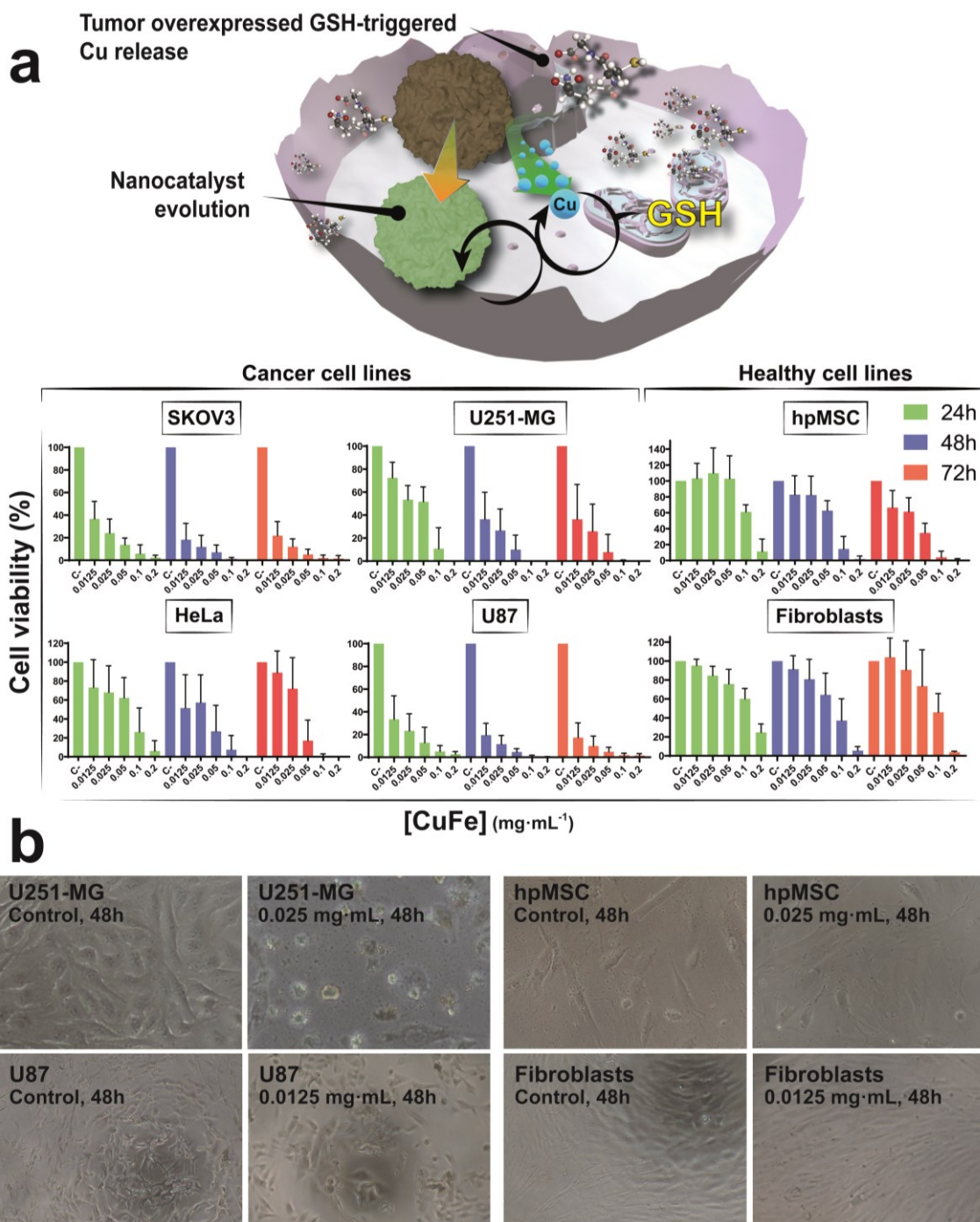


Fig. 5. Cancer cell lines with overexpressed GSH levels are affected by CuFe-triggered catalysis. (a) Cell viability study of CuFe nanocatalyst with different cancer (SKOV-3, U251-MG, HeLa and U87) and non-tumoral (hpMSC and fibroblasts) cell lines. The higher concentration of GSH in cancer cell lines enhances the action of the CuFe nanocatalyst, decreasing GSH levels while simultaneously generating superoxide species; **(b)** Optical microscopy images of tumoral (U251-MG, U87) and healthy (hpMSC, fibroblasts) cell lines at different CuFe concentrations.

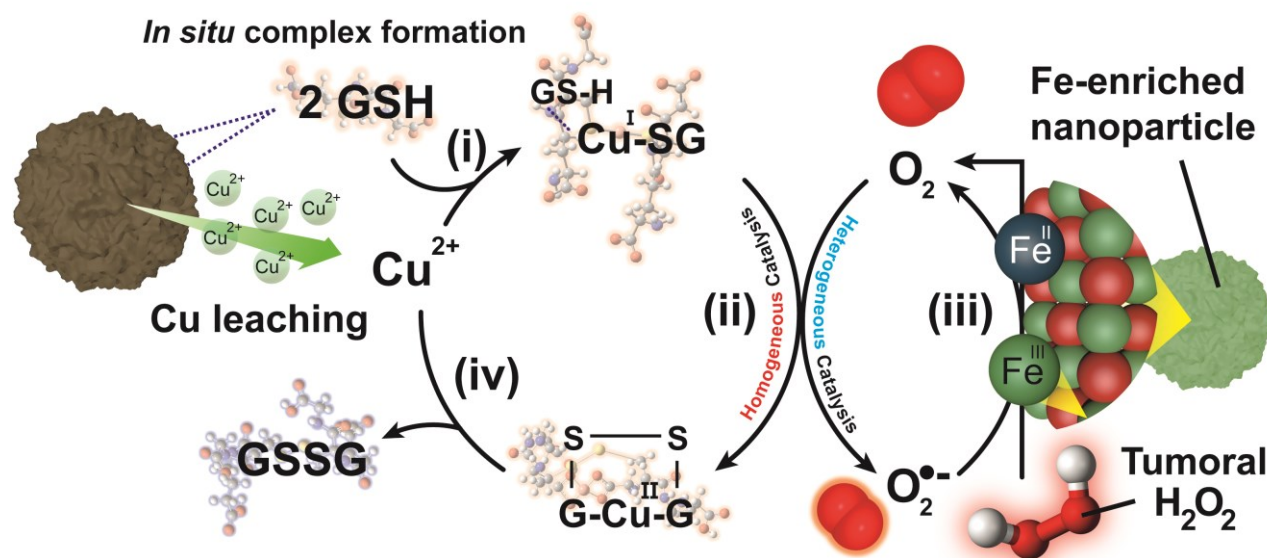


Fig. 6. Complete homogeneous-heterogeneous interplay for the CuFe nanoparticles in the presence of GSH and O_2 : (i) In a first step, GSH triggers Cu-release from the spinel nanostructure (ii) excess GSH is able to form an organometallic complex with Cu through thiol (-SH) groups to stabilize Cu^{I} (iii) Molecular O_2 accepts electrons from $\text{Cu}(\text{SG})_2$ complex to yield superoxide $\bullet\text{O}_2^-$ and $\text{Cu}(\text{GSSG})$. (iv) In a heterogeneously coupled process, as-generated $\bullet\text{O}_2^-$ donates electrons to the remaining Fe-enriched surface of the solid heterogeneous nanocatalyst in a process that generates oxygen needed for step iii. A parallel enzyme-mimicking process of H_2O_2 decomposition also takes place on the Fe-enriched catalyst, contributing additional oxygen generation.

CONCLUSIONS

Processes promoted by heterogeneous catalysts are not necessarily of a purely heterogeneous nature. Here we demonstrate that a combination of homogeneous and heterogeneous processes can originate from a copper-iron based nanocatalyst under conditions that are relevant in the tumor microenvironment. The main part of the contributing reactions take place in a homogeneous cycle catalyzed by released Cu species. The results shed light on the complexity of the processes taking place in developing fields such as Nanocatalytic Cancer Therapy. As demonstrated in this work for a CuFe hybrid nanocatalyst, lixiviation mechanisms induced by specific biomolecules with a strong presence in the TME such as GSH may lead to new catalytic scenarios where homogeneous and heterogeneous processes become interrelated events. This means that catalyst design becomes more complex, since it has to take into account the effect of environmental species on the stability of the catalyst, but also more powerful, since leaching processes can be engineered to yield synergistic

catalytic actions. Under this scenario, the design of the catalyst will consider not only its ability to favour specific surface reactions, but also its role as a reservoir for the long-term release of active ions in response to the stimuli of the chemical environment. This point of view will be key to develop novel nanoparticles capable of acting as successful bio-orthogonal catalysts.

Acknowledgements

Financial support from the European Research Council (ERC Advanced Grant CADENCE number 742684) is gratefully acknowledged. The TEM measurements were conducted at the Laboratorio de Microscopias Avanzadas, Instituto de Nanociencia y Materiales de Aragon, Universidad de Zaragoza, Spain. The synthesis of materials has been performed by the Platform of Production of Biomaterials and Nanoparticles of the NANBIOSIS ICTS, more specifically by the Nanoparticle Synthesis Unit of the CIBER in BioEngineering, Biomaterials & Nanomedicine (CIBER-BBN). J.B-A. acknowledges the Spanish Government for an FPU predoctoral contract. M. E. acknowledges the Diputacion General de Aragon (DGA) for a predoctoral contract. The authors thank Dr. Javier Calzada and Dr. Silvia Irusta for their help with UPLC and XPS measurements.

Author Contributions

J.B.-A. and J.L.H. prepared and characterized the materials. J.B.-A., M.E. and E. U. performed the experiments and analysed the data; E.U, P.M-D., J.L.H. and J.S. designed, coordinated and supervised the research and analysed the data. J.B-A, J.L.H. and J.S. wrote the paper with contribution and approval of all the authors.

REFERENCES

- 1 Ding, Y., Dai, Y., Wu, M. & Li, L. Glutathione-Mediated Nanomedicines for Cancer Diagnosis and Therapy. *Chemical Engineering Journal*, 128880, doi:<https://doi.org/10.1016/j.cej.2021.128880> (2021).
- 2 Acharya, A., Das, I., Chandhok, D. & Saha, T. Redox regulation in cancer: a double-edged sword with therapeutic potential. *Oxid Med Cell Longev* **3**, 23-34, doi:10.4161/oxim.3.1.10095 (2010).
- 3 Nelson, D. L., Lehninger, A. L. & Cox, M. M. *Lehninger Principles of Biochemistry*. (W. H. Freeman, 2008).
- 4 Balendiran, G. K., Dabur, R. & Fraser, D. The role of glutathione in cancer. *Cell Biochemistry and Function* **22**, 343-352, doi:<https://doi.org/10.1002/cbf.1149> (2004).

- 5 Traverso, N. *et al.* Role of glutathione in cancer progression and chemoresistance. *Oxid Med Cell Longev* **2013**, 972913-972913, doi:10.1155/2013/972913 (2013).
- 6 Wang, L., Huo, M., Chen, Y. & Shi, J. Tumor Microenvironment-Enabled Nanotherapy. *Advanced healthcare materials* **7**, e1701156, doi:10.1002/adhm.201701156 (2018).
- 7 Li, S. *et al.* A Nanozyme with Photo-Enhanced Dual Enzyme-Like Activities for Deep Pancreatic Cancer Therapy. *Angewandte Chemie International Edition* **58**, 12624-12631, doi:<https://doi.org/10.1002/anie.201904751> (2019).
- 8 Sun, Q. *et al.* Recent advances on endogenous/exogenous stimuli-triggered nanoplatfoms for enhanced chemodynamic therapy. *Coordination Chemistry Reviews* **451**, 214267, doi:<https://doi.org/10.1016/j.ccr.2021.214267> (2022).
- 9 Zhang, X., Lin, Y. & Gillies, R. J. Tumor pH and Its Measurement. *Journal of Nuclear Medicine* **51**, 1167, doi:10.2967/jnumed.109.068981 (2010).
- 10 Yu, L. *et al.* "Manganese Extraction" Strategy Enables Tumor-Sensitive Biodegradability and Theranostics of Nanoparticles. *Journal of the American Chemical Society* **138**, 9881-9894, doi:10.1021/jacs.6b04299 (2016).
- 11 Yue, L. *et al.* pH-Responsive, Self-Sacrificial Nanotheranostic Agent for Potential In Vivo and In Vitro Dual Modal MRI/CT Imaging, Real-Time, and In Situ Monitoring of Cancer Therapy. *Bioconjugate chemistry* **28**, 400-409, doi:10.1021/acs.bioconjchem.6b00562 (2017).
- 12 Jing, X. *et al.* Intelligent nanoflowers: a full tumor microenvironment-responsive multimodal cancer theranostic nanoplatfom. *Nanoscale* **11**, 15508-15518, doi:10.1039/C9NR04768A (2019).
- 13 Wang, S. *et al.* Arginine-Rich Manganese Silicate Nanobubbles as a Ferroptosis-Inducing Agent for Tumor-Targeted Theranostics. *ACS Nano* **12**, 12380-12392, doi:10.1021/acsnano.8b06399 (2018).
- 14 Xu, J. *et al.* Tumor Microenvironment-Responsive Mesoporous MnO₂-Coated Upconversion Nanoplatfom for Self-Enhanced Tumor Theranostics. *Advanced Functional Materials* **28**, 1803804, doi:10.1002/adfm.201803804 (2018).
- 15 Jiang, F. *et al.* Biocompatible CuO-decorated carbon nanoplatfoms for multiplexed imaging and enhanced antitumor efficacy via combined photothermal therapy/chemodynamic therapy/chemotherapy. *Science China Materials* **63**, 1818-1830, doi:10.1007/s40843-019-1397-0 (2020).
- 16 Guo, G. *et al.* Space-Selective Chemodynamic Therapy of CuFe₅O₈ Nanocubes for Implant-Related Infections. *ACS Nano* **14**, 13391-13405, doi:10.1021/acsnano.0c05255 (2020).

- 17 Xu, J. *et al.* All-in-One Theranostic Nanomedicine with Ultrabright Second Near-Infrared Emission for Tumor-Modulated Bioimaging and Chemodynamic/Photodynamic Therapy. *ACS Nano* **14**, 9613-9625, doi:10.1021/acsnano.0c00082 (2020).
- 18 Wu, H. *et al.* Smart Porous Core–Shell Cuprous Oxide Nanocatalyst with High Biocompatibility for Acid-Triggered Chemo/Chemodynamic Synergistic Therapy. *Small* **16**, 2001805, doi:<https://doi.org/10.1002/smll.202001805> (2020).
- 19 Li, Y. *et al.* Decoration of Cisplatin on 2D Metal–Organic Frameworks for Enhanced Anticancer Effects through Highly Increased Reactive Oxygen Species Generation. *ACS Applied Materials & Interfaces* **10**, 30930-30935, doi:10.1021/acsami.8b12800 (2018).
- 20 Yang, C. *et al.* Programmable NIR-II Photothermal-Enhanced Starvation-Primed Chemodynamic Therapy using Glucose Oxidase-Functionalized Ancient Pigment Nanosheets. *Small* **16**, 2001518, doi:<https://doi.org/10.1002/smll.202001518> (2020).
- 21 Gunawan, C., Teoh, W. Y., Marquis, C. P. & Amal, R. Cytotoxic Origin of Copper(II) Oxide Nanoparticles: Comparative Studies with Micron-Sized Particles, Leachate, and Metal Salts. *ACS Nano* **5**, 7214-7225, doi:10.1021/nn2020248 (2011).
- 22 Wang, Z., von dem Bussche, A., Kabadi, P. K., Kane, A. B. & Hurt, R. H. Biological and Environmental Transformations of Copper-Based Nanomaterials. *ACS Nano* **7**, 8715-8727, doi:10.1021/nn403080y (2013).
- 23 Wang, Z. *et al.* CuO Nanoparticle Interaction with Human Epithelial Cells: Cellular Uptake, Location, Export, and Genotoxicity. *Chemical Research in Toxicology* **25**, 1512-1521, doi:10.1021/tx3002093 (2012).
- 24 Eremin, D. B. & Ananikov, V. P. Understanding active species in catalytic transformations: From molecular catalysis to nanoparticles, leaching, “Cocktails” of catalysts and dynamic systems. *Coordination Chemistry Reviews* **346**, 2-19, doi:<https://doi.org/10.1016/j.ccr.2016.12.021> (2017).
- 25 Chang, M. *et al.* A Multifunctional Cascade Bioreactor Based on Hollow-Structured Cu₂MoS₄ for Synergetic Cancer Chemo-Dynamic Therapy/Starvation Therapy/Phototherapy/Immunotherapy with Remarkably Enhanced Efficacy. *Advanced Materials* **31**, 1905271, doi:<https://doi.org/10.1002/adma.201905271> (2019).
- 26 Yin, S.-Y. *et al.* Persistent Regulation of Tumor Microenvironment via Circulating Catalysis of MnFe₂O₄@Metal–Organic Frameworks for Enhanced

- Photodynamic Therapy. *Advanced Functional Materials* **29**, 1901417, doi:<https://doi.org/10.1002/adfm.201901417> (2019).
- 27 Liu, Y. *et al.* All-in-One Theranostic Nanoagent with Enhanced Reactive Oxygen Species Generation and Modulating Tumor Microenvironment Ability for Effective Tumor Eradication. *ACS Nano* **12**, 4886-4893, doi:10.1021/acsnano.8b01893 (2018).
- 28 Wang, Z. *et al.* Synthesis of one-for-all type Cu₅FeS₄ nanocrystals with improved near infrared photothermal and Fenton effects for simultaneous imaging and therapy of tumor. *Journal of Colloid and Interface Science* **592**, 116-126, doi:<https://doi.org/10.1016/j.jcis.2021.02.037> (2021).
- 29 Szatrowski, T. P. & Nathan, C. F. Production of Large Amounts of Hydrogen Peroxide by Human Tumor Cells. *Cancer Research* **51**, 794 (1991).
- 30 Wang, X., Zhong, X., Liu, Z. & Cheng, L. Recent progress of chemodynamic therapy-induced combination cancer therapy. *Nano Today* **35**, 100946, doi:<https://doi.org/10.1016/j.nantod.2020.100946> (2020).
- 31 Ge, E. J. *et al.* Connecting copper and cancer: from transition metal signalling to metalloplasia. *Nature Reviews Cancer*, doi:10.1038/s41568-021-00417-2 (2021).
- 32 Hedberg, J., Blomberg, E. & Odnevall Wallinder, I. In the Search for Nanospecific Effects of Dissolution of Metallic Nanoparticles at Freshwater-Like Conditions: A Critical Review. *Environmental Science & Technology* **53**, 4030-4044, doi:10.1021/acs.est.8b05012 (2019).
- 33 Tummanapelli, A. K. & Vasudevan, S. Ab Initio MD Simulations of the Brønsted Acidity of Glutathione in Aqueous Solutions: Predicting pKa Shifts of the Cysteine Residue. *The Journal of Physical Chemistry B* **119**, 15353-15358, doi:10.1021/acs.jpcc.5b10093 (2015).
- 34 Wall, S., Oh, J.-Y., Diers, A. & Landar, A. Oxidative Modification of Proteins: An Emerging Mechanism of Cell Signaling. **3**, doi:10.3389/fphys.2012.00369 (2012).
- 35 Nagy, P. Kinetics and mechanisms of thiol-disulfide exchange covering direct substitution and thiol oxidation-mediated pathways. *Antioxidants & redox signaling* **18**, 1623-1641, doi:10.1089/ars.2012.4973 (2013).
- 36 Rabenstein, D. L. Nuclear magnetic resonance studies of the acid-base chemistry of amino acids and peptides. I. Microscopic ionization constants of glutathione and methylmercury-complexed glutathione. *Journal of the American Chemical Society* **95**, 2797-2803, doi:10.1021/ja00790a009 (1973).

- 37 Ngamchuea, K., Batchelor-McAuley, C. & Compton, R. G. The Copper(II)-Catalyzed Oxidation of Glutathione. *Chemistry – A European Journal* **22**, 15937-15944, doi:<https://doi.org/10.1002/chem.201603366> (2016).
- 38 Speisky, H. *et al.* Cu(I)–Glutathione complex: A potential source of superoxide radicals generation. *Bioorganic & Medicinal Chemistry* **16**, 6568-6574, doi:<https://doi.org/10.1016/j.bmc.2008.05.026> (2008).
- 39 Speisky, H. *et al.* Generation of superoxide radicals by copper–glutathione complexes: Redox-consequences associated with their interaction with reduced glutathione. *Bioorganic & Medicinal Chemistry* **17**, 1803-1810, doi:<https://doi.org/10.1016/j.bmc.2009.01.069> (2009).
- 40 Speisky, H. *et al.* Cu(I)-glutathione complex: a potential source of superoxide radicals generation. *Bioorganic & medicinal chemistry* **16**, 6568-6574, doi:10.1016/j.bmc.2008.05.026 (2008).
- 41 Aliaga, M. E., Carrasco-Pozo, C., López-Alarcón, C. & Speisky, H. The Cu(I)–glutathione complex: factors affecting its formation and capacity to generate reactive oxygen species. *Transition Metal Chemistry* **35**, 321-329, doi:10.1007/s11243-010-9330-9 (2010).
- 42 Aliaga, M. E., López-Alarcón, C., Bridi, R. & Speisky, H. Redox-implications associated with the formation of complexes between copper ions and reduced or oxidized glutathione. *Journal of Inorganic Biochemistry* **154**, 78-88, doi:<https://doi.org/10.1016/j.jinorgbio.2015.08.005> (2016).
- 43 Morgan, M. T., Nguyen, L. A. H., Hancock, H. L. & Fahrni, C. J. Glutathione limits aquacopper(I) to sub-femtomolar concentrations through cooperative assembly of a tetranuclear cluster. *Journal of Biological Chemistry* **292**, 21558-21567, doi:10.1074/jbc.M117.817452 (2017).
- 44 Ciriolo, M. R., Desideri, A., Paci, M. & Rotilio, G. Reconstitution of Cu,Zn-superoxide dismutase by the Cu(I).glutathione complex. *The Journal of biological chemistry* **265**, 11030-11034 (1990).
- 45 Pearson, R. G. Hard and Soft Acids and Bases. *Journal of the American Chemical Society* **85**, 3533-3539, doi:10.1021/ja00905a001 (1963).
- 46 Moggach, S. A. *et al.* Pressure induced phase transitions in the tripeptide glutathione to 5.24 GPa: the crystal structure of glutathione-II at 2.94 GPa and glutathione-III at 3.70 GPa. **12**, 2587-2595 (2010).
- 47 Görbitz, C. J. A. C. S. A Redetermination of the Crystal and Molecular Structure of Glutathione (γL-Glutamyl-L-cysteinylglycine) at 120 K. **41**, 362-366 (1987).
- 48 Wright, W. J. A. C. The crystal structure of glutathione. **11**, 632-642 (1958).

- 49 Jelsch, C. & Didierjean, C. J. A. C. S. C. C. S. C. The oxidized form of glutathione. **55**, 1538-1540 (1999).
- 50 Kretzschmar, J., Brendler, E., Wagler, J. & Schmidt, A.-C. J. J. o. h. m. Kinetics and activation parameters of the reaction of organoarsenic (V) compounds with glutathione. **280**, 734-740 (2014).
- 51 Gao, Z. *et al.* The facile and additive-free synthesis of a cell-friendly iron (III)–glutathione complex. **49**, 10574-10579 (2020).
- 52 Qi, W. *et al.* Glutathione Complexed Fe–S Centers. *Journal of the American Chemical Society* **134**, 10745-10748, doi:10.1021/ja302186j (2012).
- 53 Corazza, A., Harvey, I. & Sadler, P. J. ¹H,¹³C-NMR and X-ray absorption studies of copper(I) glutathione complexes. *European journal of biochemistry* **236**, 697-705, doi:10.1111/j.1432-1033.1996.0697d.x (1996).
- 54 Dean, J. A. & Lange, N. A. *Lange's Handbook of Chemistry*. (McGraw-Hill, 1992).
- 55 Walsh, M. J. & Ahner, B. A. Determination of stability constants of Cu(I), Cd(II) & Zn(II) complexes with thiols using fluorescent probes. *Journal of Inorganic Biochemistry* **128**, 112-123, doi:<https://doi.org/10.1016/j.jinorgbio.2013.07.012> (2013).
- 56 Shtyrlin, V. G., Zyavkina, Y. I., Ilakin, V. S., Garipov, R. R. & Zakharov, A. V. Structure, stability, and ligand exchange of copper(II) complexes with oxidized glutathione. *Journal of Inorganic Biochemistry* **99**, 1335-1346, doi:<https://doi.org/10.1016/j.jinorgbio.2005.03.008> (2005).
- 57 Shen, X., Wang, Z., Gao, X. & Zhao, Y. Density Functional Theory-Based Method to Predict the Activities of Nanomaterials as Peroxidase Mimics. *ACS Catalysis* **10**, 12657-12665, doi:10.1021/acscatal.0c03426 (2020).
- 58 Crichton, R., Crichton, R. R. & Boelaert, J. R. *Inorganic Biochemistry of Iron Metabolism: From Molecular Mechanisms to Clinical Consequences*. (Wiley, 2001).
- 59 Ma, B. *et al.* Self-Assembled Copper–Amino Acid Nanoparticles for in Situ Glutathione “AND” H₂O₂ Sequentially Triggered Chemodynamic Therapy. *Journal of the American Chemical Society* **141**, 849-857, doi:10.1021/jacs.8b08714 (2019).
- 60 Biesinger, M. C. Advanced analysis of copper X-ray photoelectron spectra. *Surface and Interface Analysis* **49**, 1325-1334, doi:<https://doi.org/10.1002/sia.6239> (2017).
- 61 Liu, Y. *et al.* Multifunctional Magnetic Copper Ferrite Nanoparticles as Fenton-like Reaction and Near-Infrared Photothermal Agents for Synergistic

- Antibacterial Therapy. *ACS Applied Materials & Interfaces* **11**, 31649-31660, doi:10.1021/acsami.9b10096 (2019).
- 62 Wang, W., Jiang, X. & Chen, K. Iron phosphate microflowers as peroxidase mimic and superoxide dismutase mimic for biocatalysis and biosensing. *Chemical Communications* **48**, 7289-7291, doi:10.1039/C2CC32429F (2012).
- 63 Guo, S., Han, Y. & Guo, L. Mechanistic Study of Catalase- and Superoxide Dismutation-Mimic Activities of Cobalt Oxide Nanozyme from First-Principles Microkinetic Modeling. *Catalysis Surveys from Asia* **24**, 70-85, doi:10.1007/s10563-019-09290-4 (2020).
- 64 Zhang, Y. *et al.* Hollow magnetic nanosystem-boosting synergistic effect between magnetic hyperthermia and sonodynamic therapy via modulating reactive oxygen species and heat shock proteins. *Chemical Engineering Journal* **390**, 124521, doi:<https://doi.org/10.1016/j.cej.2020.124521> (2020).
- 65 Liu, C. *et al.* Biodegradable Biomimic Copper/Manganese Silicate Nanospheres for Chemodynamic/Photodynamic Synergistic Therapy with Simultaneous Glutathione Depletion and Hypoxia Relief. *ACS Nano* **13**, 4267-4277, doi:10.1021/acsnano.8b09387 (2019).
- 66 Huo, M., Wang, L., Chen, Y. & Shi, J. Tumor-selective catalytic nanomedicine by nanocatalyst delivery. *Nature Communications* **8**, 357, doi:10.1038/s41467-017-00424-8 (2017).
- 67 Zhao, Y. *et al.* Missing-Linker-Assisted Artesunate Delivery by Metal-Organic Frameworks for Synergistic Cancer Treatment. *Angewandte Chemie International Edition n/a*, doi:<https://doi.org/10.1002/anie.202112128> (2021).
- 68 Kuppusamy, P. *et al.* Noninvasive Imaging of Tumor Redox Status and Its Modification by Tissue Glutathione Levels. *Cancer Research* **62**, 307 (2002).
- 69 Weiss, J. & Humphrey, C. W. Reaction between Hydrogen Peroxide and Iron Salts. *Nature* **163**, 691-691, doi:10.1038/163691a0 (1949).
- 70 Hayyan, M., Hashim, M. A. & AlNashef, I. M. Superoxide Ion: Generation and Chemical Implications. *Chemical Reviews* **116**, 3029-3085, doi:10.1021/acs.chemrev.5b00407 (2016).

Supplementary Information

Leveraging the interplay between homogeneous and heterogeneous catalytic mechanisms: copper-iron nanoparticles working under chemically relevant tumor conditions

Javier Bonet-Aleta^{a,b,c}, Miguel Encinas^{a,b,c}, Esteban Urriolabeitia^d, Pilar Martin-Duque^{b,e,f,g}, Jose L. Hueso^{a,b,c}, Jesus Santamaria^{a,b,c,f}

^aInstitute of Nanoscience and Materials of Aragon (INMA), CSIC-Universidad de Zaragoza, Campus Río Ebro, Edificio I+D, C/ Poeta Mariano Esquillor, s/n, 50018, Zaragoza, Spain.

^bNetworking Research Center in Biomaterials, Bioengineering and Nanomedicine (CIBER-BBN), Madrid, Spain. Instituto de Salud Carlos III; 28029, Madrid, Spain.

^cDepartment of Chemical and Environmental Engineering; University of Zaragoza, Spain; Campus Rio Ebro, C/María de Luna, 3, 50018 Zaragoza, Spain.

^dInstituto de Síntesis Química y Catálisis Homogénea, ISQCH (CSIC-Universidad de Zaragoza), 50009 Zaragoza, Spain.

^eInstituto Aragonés de Ciencias de la Salud (IACS), Avenida San Juan Bosco, 13, 50009 Zaragoza, Spain.

^fInstituto de Investigación Sanitaria (IIS) Aragón, Avenida San Juan Bosco, 13, 50009 Zaragoza, Spain.

^gFundación Araid. Av. de Ranillas 1-D, 50018 Zaragoza, Spain.

TABLE OF SUPPLEMENTARY CONTENTS

| | |
|--|-----------|
| S1. Chemicals and Materials..... | 28 |
| S2. Characterization techniques. | 28 |
| S3. Synthesis of CuFe-DMSA nanoparticles. | 28 |
| S4. Metal leaching study by Microwave Plasma-Atomic Emission Spectroscopy. | 29 |
| S5. ¹HNMR-study of CuFe-GSH interaction. | 29 |
| S6. Mass spectroscopy analysis of the reaction..... | 30 |
| S7. Catalytic GSH depletion..... | 30 |
| S8. UPLC-PDA equipment for GSH quantification. | 30 |

| | |
|--|----|
| S9. Generation of superoxide radicals $\bullet\text{O}_2^-$ | 30 |
| S10. Analysis of O_2 consumption/generation | 31 |
| S11. Cell culture conditions and study of CuFe cytotoxicity | 31 |
| S12. References | 48 |
| | |
| Figure S1. DOSY spectra of GSH GSSG standards.. | 32 |
| Figure S2. DOSY spectra of (a) CuCl_2 +GSH and (b) CuFe+GSH (pH=7.4) | 33 |
| Figure S3. $^1\text{H-NMR-DOSY}$ analysis from FeCl_3 +GSH experiments. | 34 |
| Figure S4. HRMS-ESI analysis of different species found in FeCl_3 +GSH mixture. | 35 |
| Figure S5. MS-ESI analysis of CuFe+GSH (pH = 7.40) | 36 |
| Figure S6. Detection of $\bullet\text{O}_2^-$ using DPBF probe.. | 37 |
| Figure S7. O_2 consumption experiment of CuFe + 5 mM GSH | 38 |
| Figure S8. $^1\text{H-NMR-DOSY}$ analysis from CuFe+GSH experiments at pH = 5.80. | 39 |
| Figure S9. MS-ESI analysis of CuFe+GSH at pH = 5.80..... | 40 |
| Figure S10. GSH catalytic oxidation at pH = 3.60 in the presence of CuFe..... | 41 |
| Figure S11. MS-ESI analysis of CuFe+GSH reaction at pH = 3.60 | 42 |
| Figure S12. XRD pattern obtained from CuFe after reaction with 5 mM of GSH . | 43 |
| Figure S13. $\bullet\text{OH}$ generation experiment of Fe-enriched catalyst | 44 |
| Figure S14. CuFe-DMSA synthesis scheme..... | 45 |
| Figure S15. Size distribution of CuFe after/before DMSA functionalization | 46 |
| | |
| Table S1. Elemental composition of CuFe surface measured by XPS before GSH reaction. | 47 |
| Table S2. XPS quantification of the different Fe and Cu species present on the catalyst surface before reaction with GSH..... | 47 |
| Table S3. Elemental composition of CuFe surface measured by XPS after GSH reaction. | 47 |
| Table S4. XPS quantification of the different Fe and Cu species present on the catalyst surface after reaction with GSH..... | 47 |
| Table S5. GSH standards composition employed to analyze GSH-catalytic experiments..... | 48 |

S1. Chemicals and Materials. Iron (III) chloride hexahydrate ($\text{FeCl}_3 \cdot 6\text{H}_2\text{O}$, 97%), copper (II) chloride dihydrate ($\text{CuCl}_2 \cdot 2\text{H}_2\text{O}$, $\geq 99.0\%$), sodium acetate anhydrous (CH_3COONa , 99.0 %), Bovine Serum Albumin (BSA), ethylene glycol (EG), Dimercaptosuccinic Acid (DMSA, 99.0 %), Glutathione, Glutathione oxidized (GSSG, $\geq 98.0\%$ HPLC), 5,5'-Dithiobis(2-nitrobenzoic acid) (DNTB), hydrogen peroxide (H_2O_2 , 33% v/v), sodium bicarbonate (NaHCO_3 , 99%), Methylene Blue (MB, ≥ 95.0) were purchased from Sigma Aldrich.. Acetonitrile (ACN) was purchased from WVR (Avantor). UPLC grade water was obtained from a Milli-Q Advantage A10 System with resistivity of 18.2 m Ω (Merk Millipore, Germany).

S2. Characterization techniques. Transmission electron microscopy (TEM) was performed using a FEI TECNAI T20 microscope operated at 200 keV. High-resolution transmission electron microscopy (HRTEM) was performed using a FEI Titan (80–300 kV) microscope at an acceleration voltage of 300 kV. In both cases samples were prepared by drop casting 5 μL of the nanoparticle suspension on a holey carbon TEM grid. UV-vis spectra were obtained on a UV–vis double beam spectrophotometer Jasco V67. X-ray photoelectron spectroscopy (XPS) was performed with an Axis Supra spectrometer (Kratos Tech). The samples were mounted on a sample rod placed in the pretreatment chamber of the spectrometer and then evacuated at room temperature. The spectra were excited by a monochromatized Al K α source at 1486.6 eV and subsequently run at 8 kV and 15 mA. A survey spectrum was measured at 160 eV of pass energy, and for the individual peak regions, spectra were recorded with a pass energy of 20 eV. Analysis of the peaks was performed with the CasaXPS software using a weighted sum of Lorentzian and Gaussian component curves after Shirley background subtraction. The binding energies were referenced to the internal C 1s standard at 284.5 eV. X-ray diffraction patterns were obtained in a PANalytical Empyrean equipment in Bragg-Brentano configuration using CuK α radiation and equipped with a PIXcel1D detector. ^1H spectra (D_2O) were recorded at 25 °C using a Bruker Avance 400 MHz NMR spectrometer with TMS as the internal standard and deuterated water as solvent in a 5 mm QNP probe. Nanoparticle Tracking Analysis was measured on Malvern Nanosight 300.

S3. Synthesis of CuFe-DMSA nanoparticles. CuFe_2O_4 nanoparticles were synthesized via templated-growth method. Firstly, 250 mg of BSA were dissolved in 2.5 mL of milliQ water and consequently 12.5 mL of Ethylene glycol were added. After that, 270.0 mg of $\text{FeCl}_3 \cdot 6\text{H}_2\text{O}$, 85.0 mg of CuCl_2 and 375.0 mg of CH_3COONa were added into the reaction vessel. Reaction was left to stir 2 h at room temperature to ensure a correct binding of BSA-nucleophile groups to the metallic ions. Then, the reaction was transferred to a Teflon autoclave

and the temperature was set to 180°C for 24 h. Finally, the product was centrifuged at 12 000 rpm for 20 min. 20 mL of a 25 mM solution of DMSA were poured to the reaction pellet and the dispersion was assisted with ultrasonication. 5 mL of 0.7 M NaOH solution were added to ensure the correct DMSA dissolution to decorate the nanocatalyst surface. The final product was purified by two centrifugation cycles at 12 000 rpm for 20 min. The nanocatalyst was stored at 4°C for further use. CuFe nanocatalysts were synthesized using Bovine Serum Albumin (BSA) as template^{1,2} and Ethylene glycol (EG) as a solvent to modulate particle size³. The abundance of nucleophile functional groups in the BSA (-COO-, -NH₂) can chelate the metal ions (Cu²⁺, Fe³⁺) and serve as starting point to growth the nanostructure. Although the distribution size of the nanoparticles is homogeneous, these nanoparticles suffer from aggregation in aqueous media, which may hinder cell internalization⁴. As shown previously by Miguel-Sancho et al.⁵, DMSA functionalization enhanced the dispersion and stability of the nanoparticles in aqueous media (**Fig. S14-15**). The synthesis of these materials has been performed at the Platform of Production of Bio-materials and Nanoparticles of the NANBIOSIS ICTS, more specifically by the Nanoparticle Synthesis Unit of the CIBER in BioEngineering, Biomaterials & Nanomedicine (CIBER-BBN).

S4. Metal leaching study by Microwave Plasma-Atomic Emission Spectroscopy (MP-AES).

Each solution was prepared in an eppendorf tube with CuFe-DMSA nanoparticle at a concentration of 0.1 mg/mL (total volume = 1 mL). The different solutions were introduced in an Eppendorf thermoshaker at 37°C and constant stirring of 400 rpm. At every time point (2h, 4h, 6h 24h), samples were centrifuged at 13300 rpm during 30', and the supernatants were collected for further analysis. The nanoparticle pellet was resuspended with the corresponding solution, until the next analysis cycle, where the procedure was repeated. At the experiment endpoint, the supernatant samples were analyzed together with final nanoparticle pellet, to close mass balances and elucidate how much metal moved to the solution. All the samples were digested with HCl:HNO₃ (3:1) mixture overnight. Cu and Fe concentrations were determined through the analysis with Agilent 4100 MP-AES.

S5. ¹H-NMR-study of CuFe-GSH interaction.

The interaction study of leached metals (Cu, Fe) with GSH was performed by the ¹H-NMR and DOSY analysis of different reaction mixtures. For CuCl₂-GSH experiments, the pH was fixed to 7.4 (buffer Na₂HPO₄/KH₂PO₄) and the molar ratio CuCl₂:GSH was set to 1:4 ([GSH]=20mM, [CuCl₂·2H₂O]=5mM). For FeCl₃-GSH experiments, the pH was not fixed (pH = 3.60) and the molar ratio FeCl₃:GSH was set to 1:4 ([GSH]=20mM, [FeCl₃·6H₂O]=4mM). The reaction mixtures were analyzed after incubation for 5 minutes. For CuFe+GSH experiments, molar ratio

CuFe:GSH was 1:44 ([GSH]=20 mM, [CuFe₂O₄]=0.5 mM). Reaction were incubated at pH = 7.4 (Na₂HPO₄/KH₂PO₄) and pH = 3.70 (free pH) for 3 and 24 h. All samples were filtered before analysis.

S6. Mass spectroscopy analysis of the reaction. ESI (ESI+) mass spectra were recorded using an Esquire 3000 ion-trap mass spectrometer (Bruker Daltonic GmbH) equipped with a standard ESI/APCI source. Samples were introduced by direct infusion with a syringe pump. Nitrogen served both as the nebulizer gas and the dry gas. The HRMS mass spectra were recorded using an MicroToF Q, API-Q-ToF ESI with a mass range from 20 to 3000 m/z and mass resolution 15000 (FWHM). Samples prepared for ¹H-NMR/DOSY experiments were analyzed by using this methodology.

S7. Catalytic GSH depletion. Catalytic activity towards GSH oxidation of CuFe-DMSA nanoparticles was evaluated according to the following protocol. 5 mM of GSH were mixed with 0.1 mg·mL⁻¹ of CuFe-DMSA in a total volume of 2.5 mL. GSH concentration at different reaction times was measured by UPLC-PDA. 20 µL of reaction were mixed with 100 µL of 5,5'-Disulfaneylbis(2-nitrobenzoic acid) (DTNB) and 880 µL of 0.01 M 2-Amino-2-hydroxymethyl-propane-1,3-diol (TRIS).

S8. UPLC-PDA equipment for GSH quantification. GSH analysis were performed on Waters ACQUITY system H-Class which consisted of a binary pump, an autosampler, a column thermostat and a photodiode array (PDA) detector. This system is coupled to a PhotoDiode Array (PDA) detector to monitor absorbance from derivatized GSH at 412 nm during analysis time. Data acquisition and processing were performed by using MASSLYNX software (Waters Corporation USA). In order to analyze GSH from derivatized samples as describe below, chromatographic separation was performed using an ACQUITY UPLC BEH C18 column (130 Å, 1.7 µm 2.1 x 50 mm, from WATERS) at 40°C under an isocratic flow of 0.3 mL·min⁻¹ containing 50% acetonitrile, 50% milli Q water.

S9. Generation of superoxide radicals •O₂⁻. 1,3-Diphenylisobenzofuran (DPBF) was employed as a probe to measure the production of •O₂⁻ during homogeneous GSH oxidation. 20 µL of 10 mM DPBF solution (in Ethanol) were added to 2.5 mL of a mixture Ethanol:PBS(X1) 2:1. Catalyst and GSH concentration were 0.1 mg·mL⁻¹ and 5 mM, respectively. UV-vis analysis of remaining DPBF was performed after centrifuging the sample (100 µL of reaction + 400 µL mixture Ethanol:PBSX1) at 13 000 rpm for 5'.

S10. Analysis of O₂ consumption/generation. Molecular oxygen was measured with a NeoFox oximeter equipped with FOSPOR-R probe. In order to analyze the O₂-generation capabilities of the remaining nanoparticle, CuFe (0.1 mg·mL⁻¹) was incubated with 5 mM of GSH (pH = 7.40) for 3 h to induce selective Cu-release. The solution was centrifuged at 13300 rpm for 10' to separate homogeneous and heterogeneous catalysts to analyze their individual catalytic activity towards O₂ production using [H₂O₂]₀ = 1 mM.

S11. Cell culture conditions and study of CuFe cytotoxicity.

In order to assess the effect that these nanoparticles produced on the chosen cell lines, a viability assay on 96 well plates was carried out. Briefly, cells were seeded at different densities depending on their type (3000 cells/well for tumoral cell lines, i.e. U251-MG, SKOV-1, HeLa, U87-MG and 4000 cells/well for healthy cell lines, i.e. hpMSC and fibroblasts), using Dulbecco's Modified Eagle Medium (DMEM), supplemented with 1% L-Glutamine, 1% PSA (Penicillin, Streptomycin, Amphotericin), and 10% Fetal Bovine Serum (FBS); in the case of hpMSC, DMEM medium was also supplemented with Fibroblast Growth Factor 2 (FGF-2) at 5 µg/mL.

24h after the seeding, the wells were treated with CuFe nanoparticles, in such a way that the supernatant in each well was replaced with a suspension of CuFe nanoparticles in DMEM (DMEM + FGF-2 for hpMSC) at different concentrations, ranging from 0.2 to 0.0125 mg/mL.

After 24, 48 and 72h of incubation, the wells were washed with Dulbecco's Phosphate Buffered Saline (DPBS), and then, a solution of Blue Cell Viability Reagent in DMEM (10% v/v) was used to assess the cytotoxic effect of these nanoparticles on the different cell lines. After 1h of incubation with the Blue Cell Viability Reagent at 37°C, the signal was measured with a BioTek plate reader, exciting at 528 nm and measuring the emission at 590 nm.

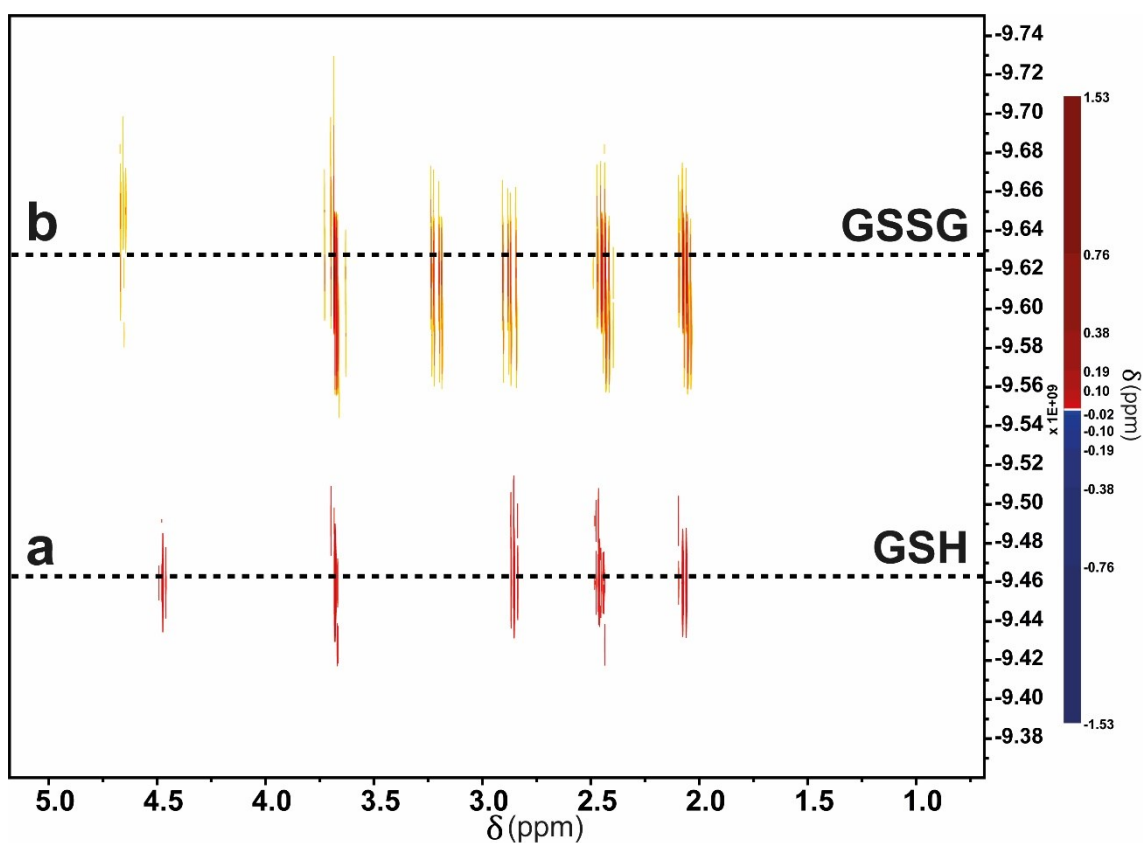


Figure S1. DOSY spectra of (a) GSH (down) and (b) GSSG (top) standards. Molecular size differences between reduced (GSH) and oxidized GSH (GSSG) translate into different diffusion coefficients (D) of the molecule. Following this trend, determined D for GSH is larger in comparison to GSSG.

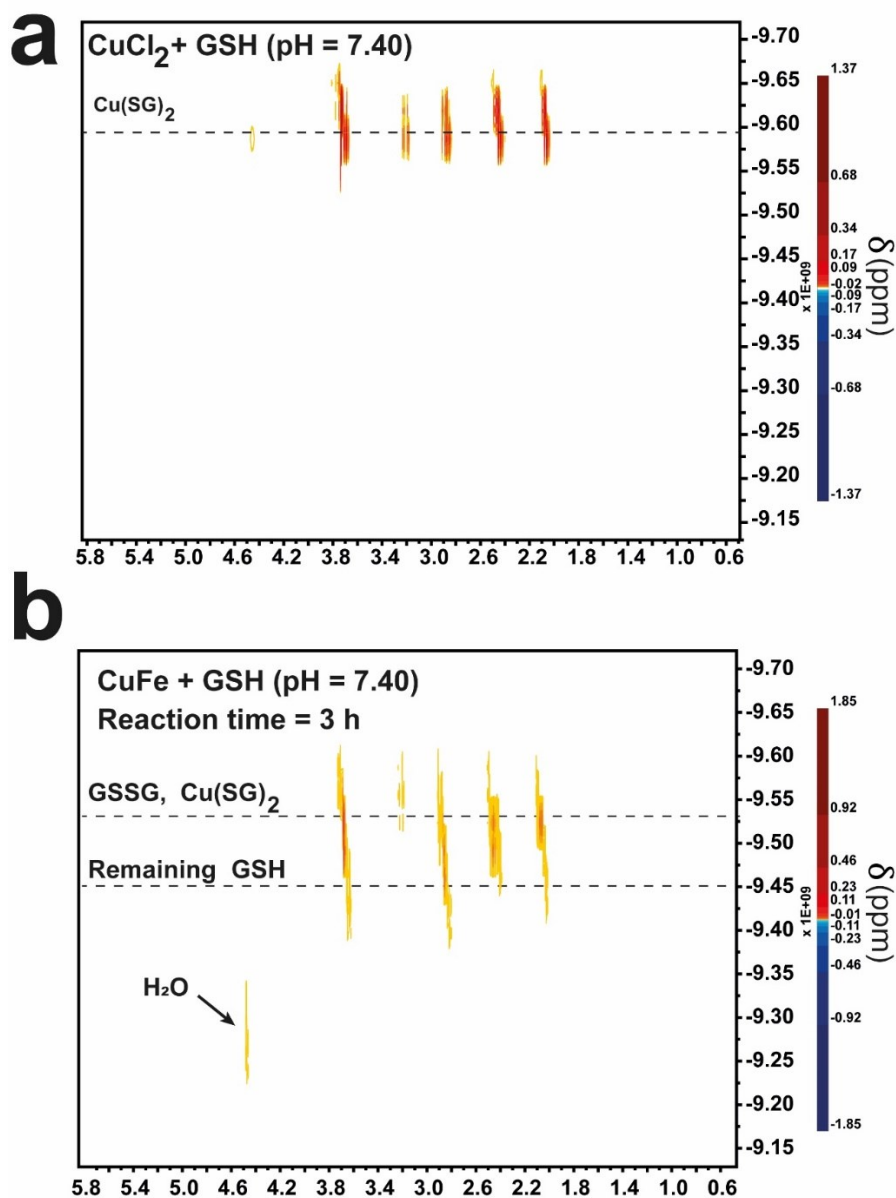


Figure S2. Comparison of diffusion coefficients of (a), $\text{CuCl}_2 + \text{GSH}$ (red) and (b) $\text{CuFe} + \text{GSH}$ (3h) (purple). Reaction conditions $[\text{GSH}] = 20 \text{ mM}$, $\text{pH} = 7.0$ ($\text{HPO}_4^{2-}/\text{H}_2\text{PO}_4$), $T = 25 \text{ }^\circ\text{C}$, reaction time = 3h. (a) DOSY spectra corresponding to the mixture $\text{CuCl}_2 + \text{GSH}$ indicate the generation of $\text{Cu}(\text{SG})_2$ complex and GSSG, which possess a similar molecular size and therefore a similar D is obtained. (b) DOSY spectra of $\text{CuFe} + \text{GSH}$ reaction at $\text{pH} = 7.40$ at 3h. As reaction is not over at this time, some remaining GSH appears at low D values (highlighted in dashed line). Moreover, as GSH and GSSG/ $\text{Cu}(\text{SG})_2$ possess same signals for some H ($\delta = 3.70 \text{ ppm}$, $\delta = 2.85 \text{ ppm}$, $\delta = 2.45 \text{ ppm}$ and $\delta = 2.05 \text{ ppm}$), DOSY signals appear wider. A similar signal with a calculated D of $4.00 \cdot 10^{-10} \text{ m}^2 \cdot \text{s}^{-1}$ in comparison with $\text{CuCl}_2 + \text{GSH}$ mixture is obtained under conditions that favour leaching of Cu, suggesting the formation of $\text{Cu}(\text{SG})_2$ complex *in situ* using the Cu released from the nanoparticle.

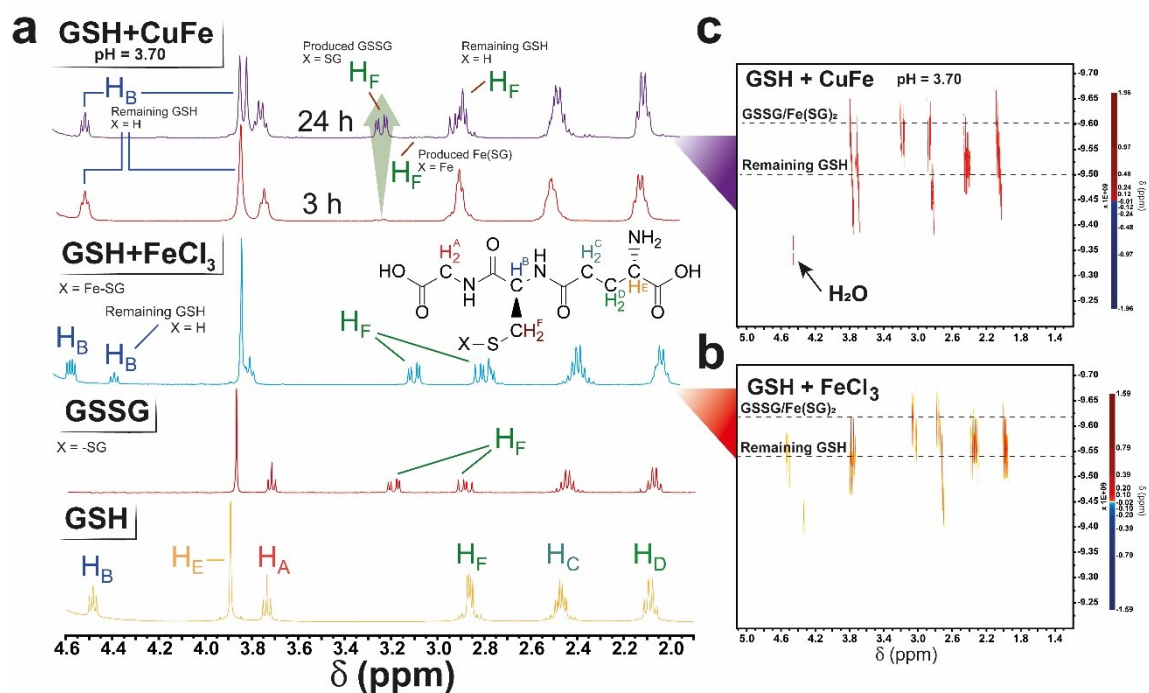


Figure S3. (a) ¹H-NMR analysis from FeCl₃+GSH experiments. Generation of Fe-SG complex entails the splitting of HF signals at 3.04 and 2.76 ppm. Analysis of reaction supernatant at 3 h reveals a small amount of GSSG produced in comparison with CuFe+GSH at pH = 7.40 consequence of slower reaction kinetics of Fe-homogeneous catalysis of GSH oxidation. However, after 24 h of reaction, a larger amount of Cu has been released and the reaction rate increases; (b) DOSY analysis of GSH+FeCl₃ mixture reveals the formation of a product with a D close to GSSG, while an important amount of GSH is still present in the solution (confirmed by ¹H-NMR in Fig. S3a). (c) DOSY spectra of CuFe+GSH at pH = 3.70

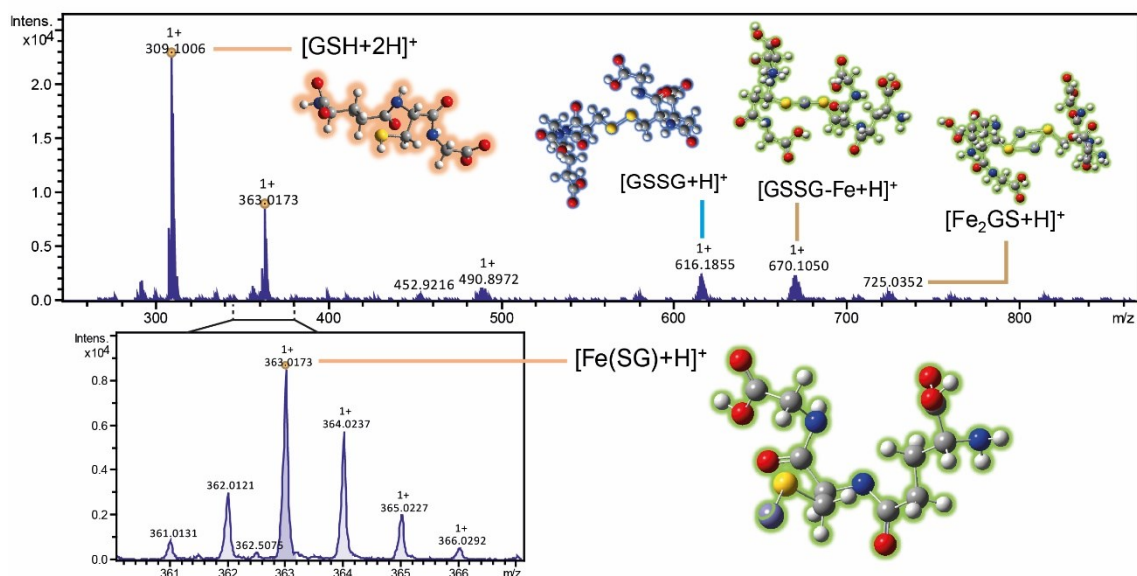


Figure S4. HRMS-ESI analysis of different species found in FeCl_3 +GSH mixture (pH = 3.60). Remaining GSH is found at $m/z = 309.1006$ ($[\text{GSH}+\text{H}]^+$), which is consistent with an important fraction of GSH still present in the solution detected by ^1H -NMR (Fig. S3). $[\text{Fe}(\text{SG})_x]$ complexes are detected at $m/z = 363.0173$ ($[\text{Fe}(\text{SG})+\text{H}]^+$) and $m/z=670.1050$ ($[\text{Fe}(\text{GSSG})+\text{H}]^+$) Polynuclear species are also detected at 725.0352 ($[[\text{Fe}(\text{SG})]_2+\text{H}]^+$).

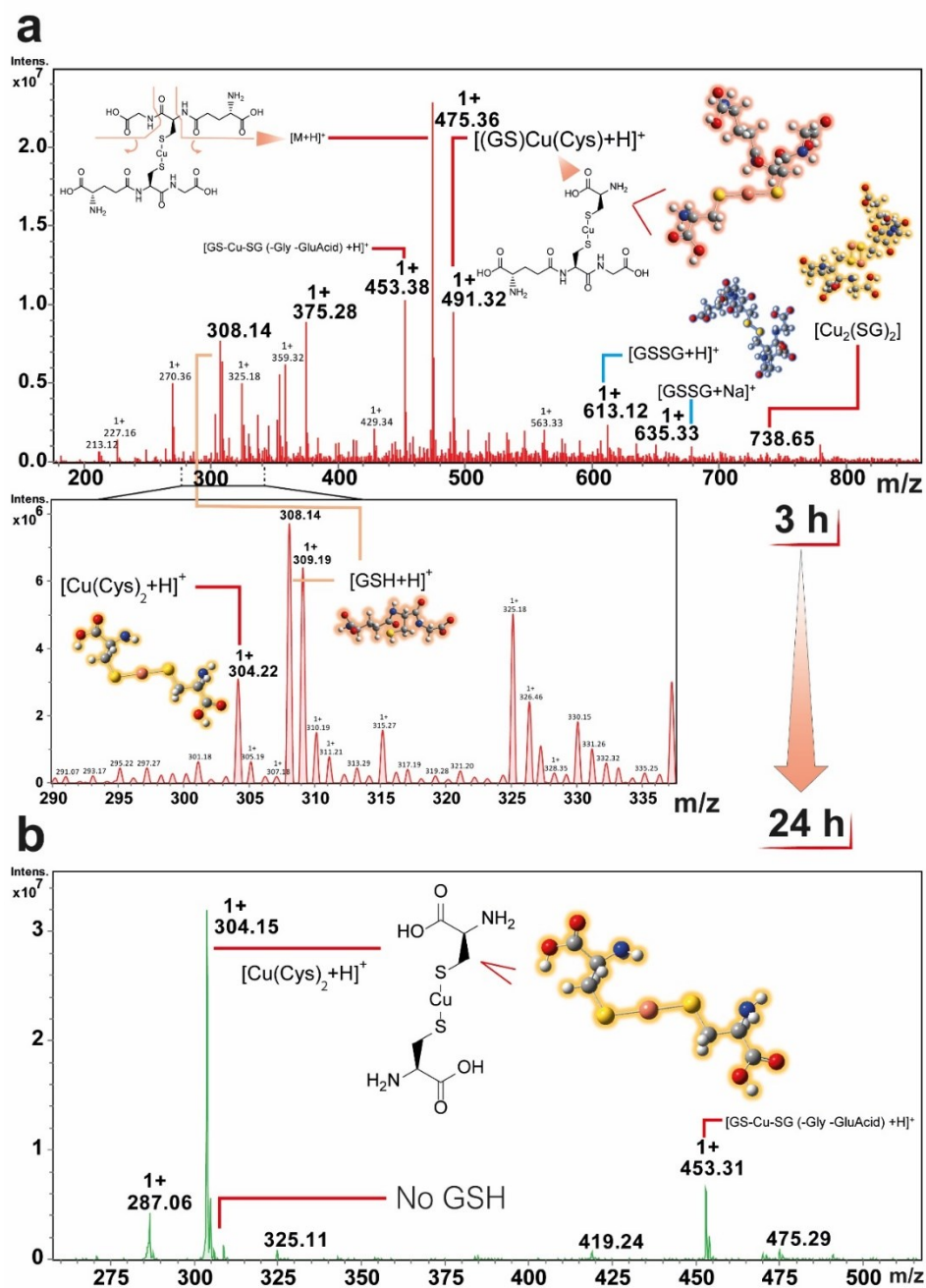


Figure S5. MS-ESI analysis of CuFe+GSH (pH = 7.40) at different reaction times: (a) 3h and (b) 24h. After 3 hours of reaction unreacted GSH and reaction product, GSSG signals at $m/z = 308$ and $m/z = 613$ are present in the spectra, in agreement with $^1\text{H-NMR}$ results. Different fragments from the $[\text{Cu}(\text{SG})_2]^+$ complex were found at $m/z = 491.32$ ($[\text{Cu}(\text{SG})(\text{Cys})]^+$), 453.38 ($[\text{Cu}(\text{SG})(\text{SG})\text{-Glutamic Acid-Glycine}]^+$) and 304.27 $[\text{Cu}(\text{Cys})_2]^+$, with the Cu-S bond always present. Analysis of the reaction supernatant at reaction time 24 h revealed the total consumption of GSH, according to $^1\text{H-NMR}$ analysis and the prominence of the $[\text{Cu}(\text{Cys})_2]^+$ fragment. We assume that the nanoparticle affects to the MS fragmentation pattern, as we were not able to detect those fragments by $^1\text{H-NMR}$.

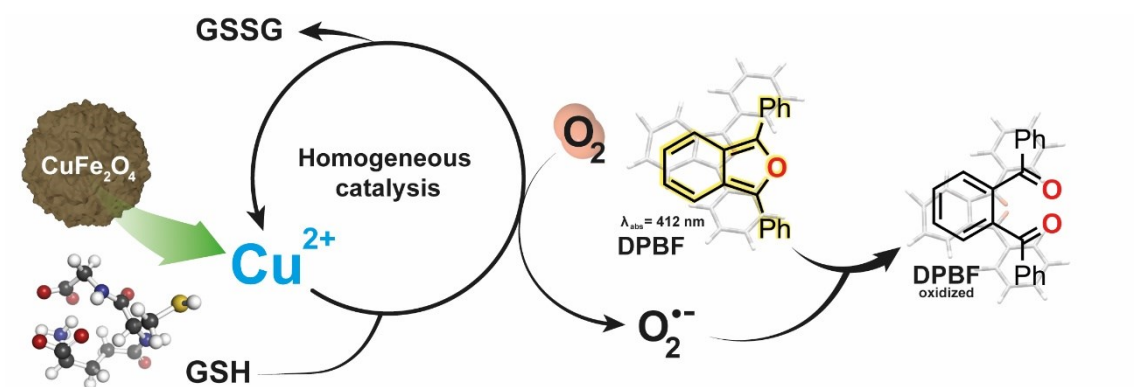


Figure S6. Detection of $\cdot\text{O}_2^-$ using DPBF probe. In the presence of GSH, Cu^{2+} is released to the media and homogeneous oxidation of GSH occur. $\cdot\text{O}_2^-$ is produced in the process and preferentially oxidizes DPBF, which absorbs at 412 nm, to 1,2-dibenzoylbenzene, a colorless molecule.

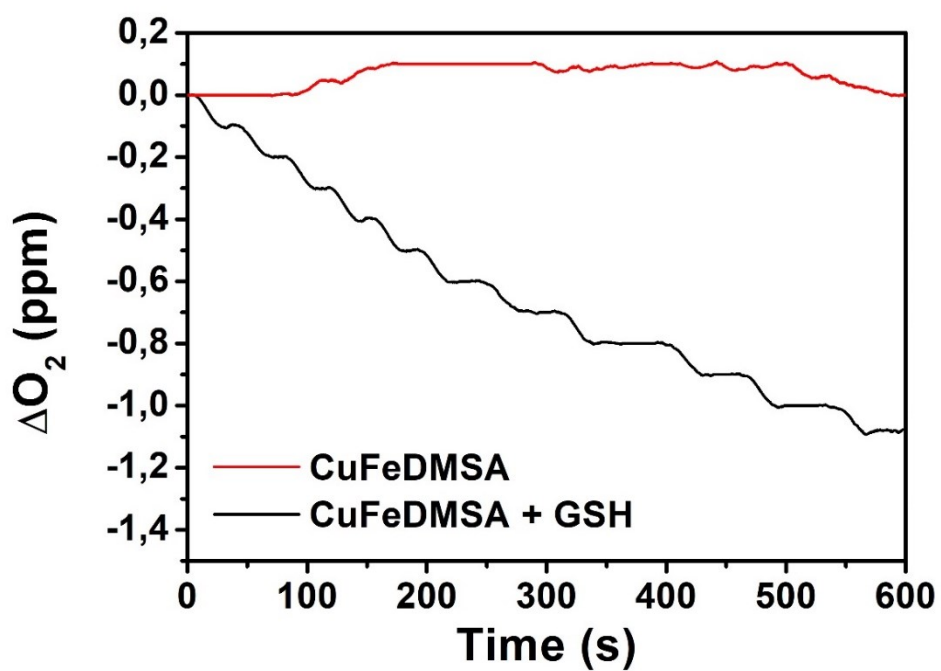


Figure S7. O_2 consumption in the presence of CuFe with or without the addition of 5 mM GSH. $[CuFe] = 0.1 \text{ mg}\cdot\text{mL}^{-1}$, $\text{pH} = 7.40$ (adjusted with $\text{HPO}_4^{2-}/\text{H}_2\text{PO}_4^-$). The decrease of O_2 levels in solution once CuFe and GSH are mixed corresponds to its role as electron acceptor in the homogeneous GSH oxidation.

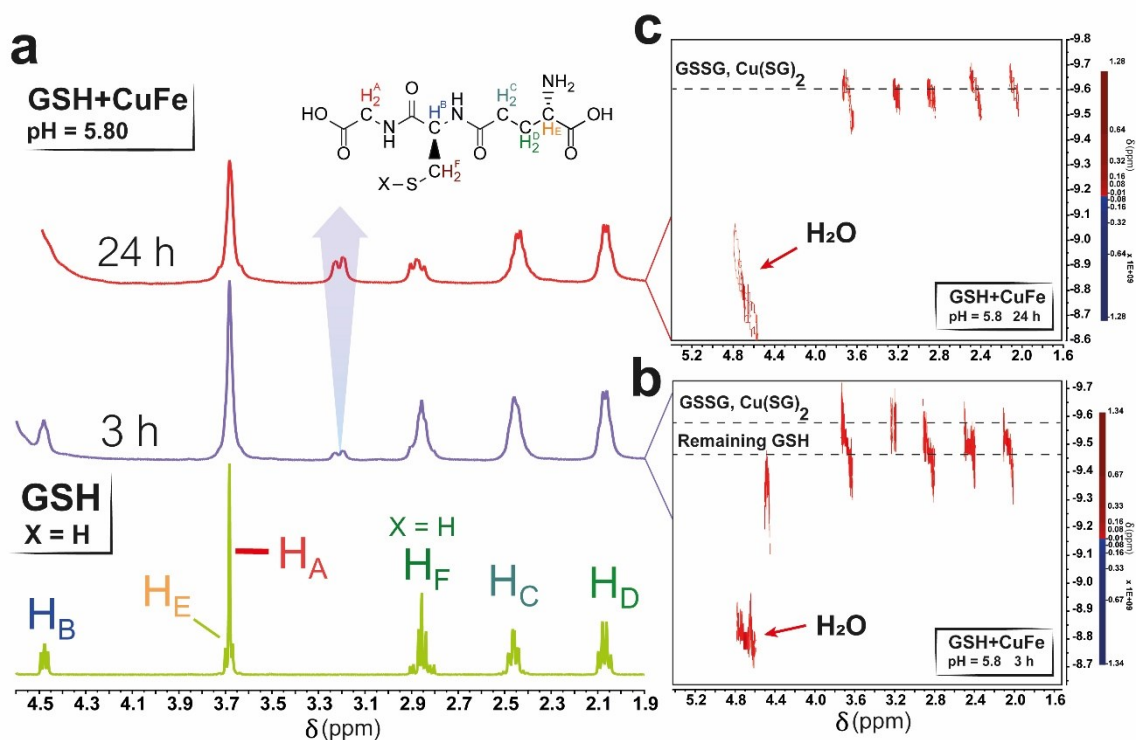


Figure S8. (a) 1H -NMR analysis from CuFe+GSH experiments at pH = 5.80. A similar behavior in comparison with CuFe+GSH at pH = 7.40 is found at tumor-characteristic pH. After 3h of reaction, a characteristic signal of GSSG/Cu(SG)₂ at 3.22 ppm appears as consequence of modification of -CH₂- close to -SH group. The reaction is complete after 24 h, as no signal of GSH is present at 4.5 ppm. (b) DOSY spectra of GSH+CuFe mixture at pH = 5.80 (HPO₄²⁻/H₂PO₄⁻), presenting both signals from GSH and GSSG/Cu(SG)₂ (c) DOSY spectra of GSH+CuFe (pH = 5.8) after 24 h of reaction, with the signal of GSH disappeared. Molecular species with a D similar to GSSG/Cu(SG)₂ are detected after 24h of reaction.

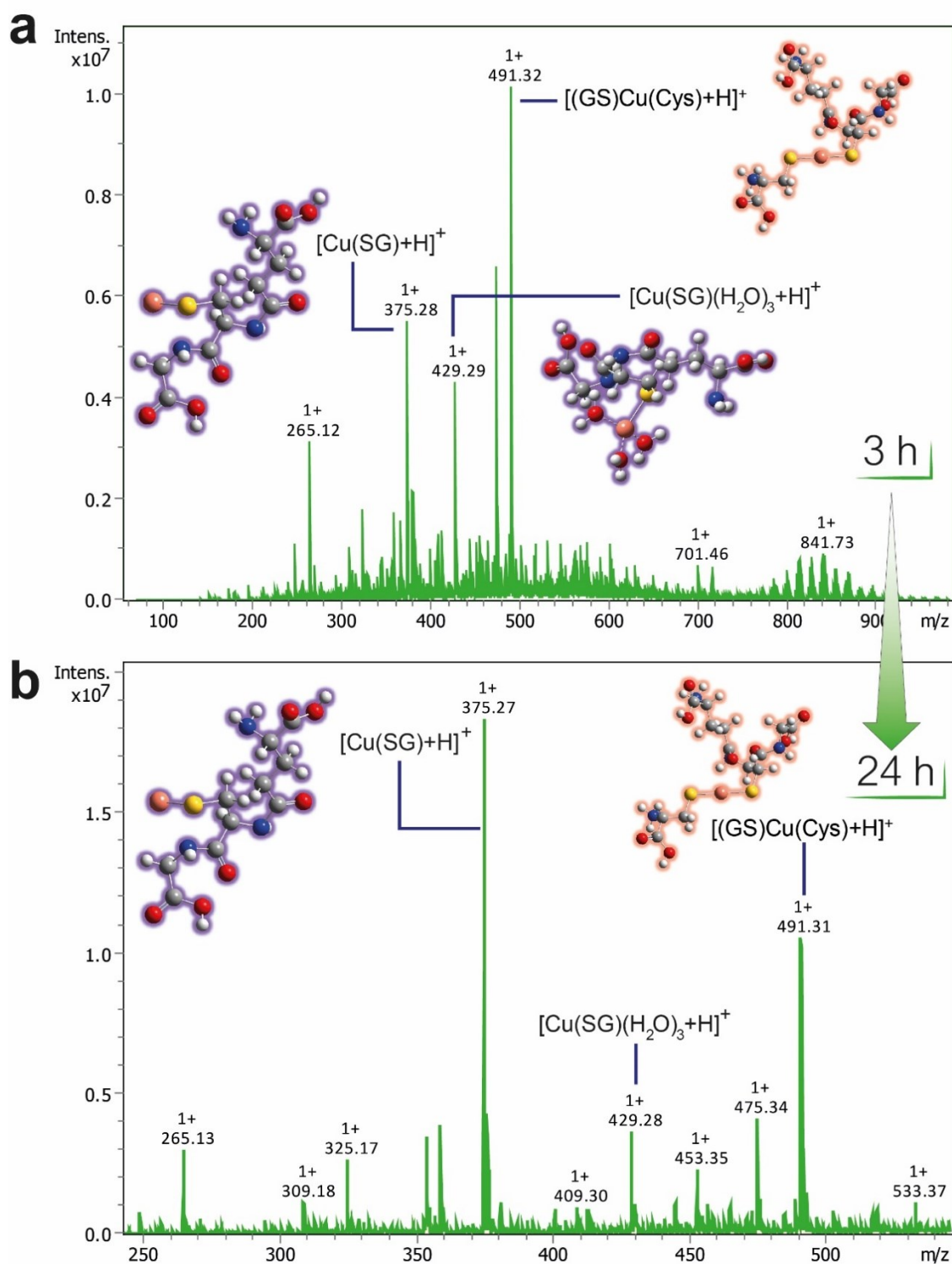


Figure S9. MS-ESI analysis of CuFe+GSH (pH = 5.80) at reaction time (a) 3h and (b) 24h. $[\text{Cu}(\text{SG})_2]^+$ -derived fragments are present at $m/z = 375.28$ ($[\text{Cu}(\text{SG})+\text{H}]^+$), 429.29 ($[\text{Cu}(\text{SG})(\text{H}_2\text{O})_3+\text{H}]^+$) and 491 ($[(\text{GS})\text{Cu}(\text{Cys})+\text{H}]^+$). Analysis of the reaction supernatant at reaction time 24 h revealed the total consumption of GSH, according to $^1\text{H-NMR}$ analysis and the prominence of a $[\text{Cu}(\text{SG})]$ fragment.

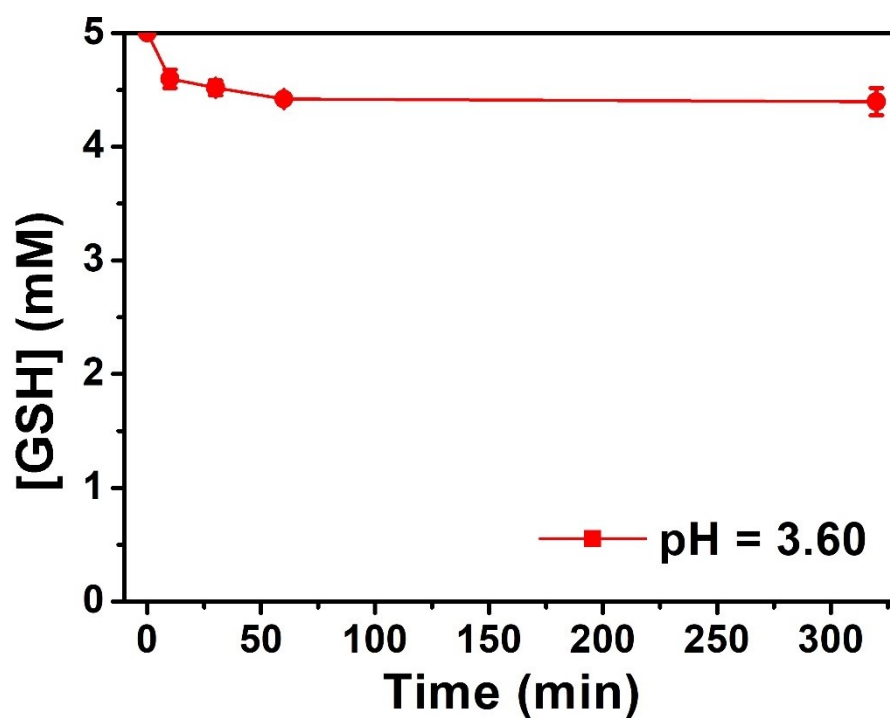


Figure S10. Monitoring of GSH levels at pH = 3.60 in the presence of CuFe catalyst, showing a slight decrease in GSH concentration (in comparison with reaction at pH = 5.80 or 7.40) at early reaction time (320 minutes). Results are in agreement with ^1H -NMR/DOSY experiments (Fig. S3a-c) indicating that GSH was present in the reaction after 3h of reaction.

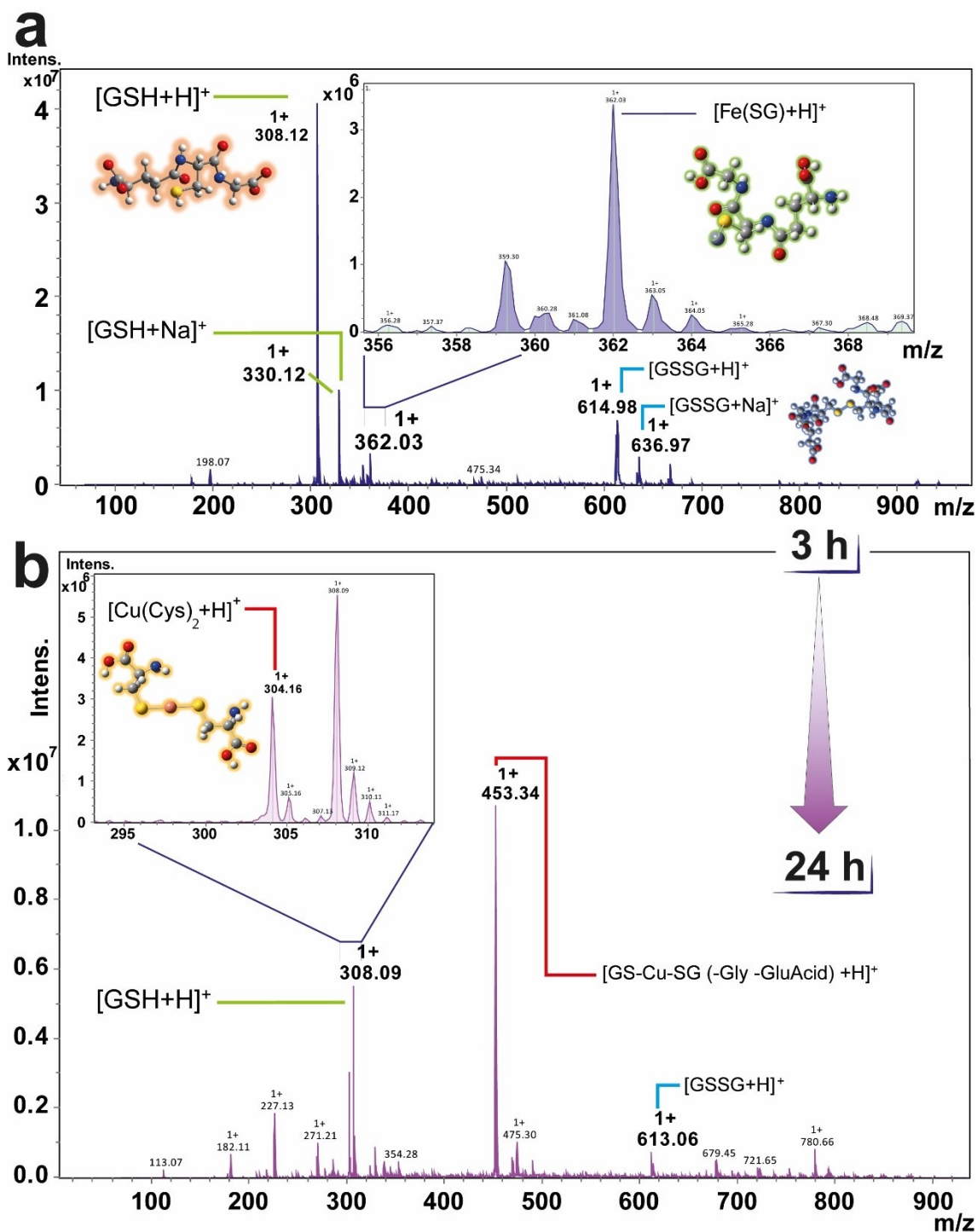


Figure S11. MS-ESI analysis of CuFe+GSH reaction (pH = 3.60) at (a) 3 h and (b) 24 h. $[\text{Fe}(\text{SG})+\text{H}]^+$ complex formed by Fe leached in the reaction at acidic pH is found at $m/z = 362.03$. Remaining GSH signal ($m/z = 308.19$, $[\text{GSH}+\text{H}]^+$ and $m/z = 330.12$ $[\text{GSH}+\text{Na}]^+$) is attributed to slow kinetics of Fe-catalytic oxidation of GSH. Analysis of the reaction at 24 h reveals the generation of $[\text{Cu}(\text{SG})_2]^+$ as fragments of $[\text{Cu}(\text{cys})_2]^+$ and $[\text{Cu}(\text{SG})\text{-Gly-GluAcid}]$ appears in the HRMS-ESI at $m/z = 304$ and 453, respectively.

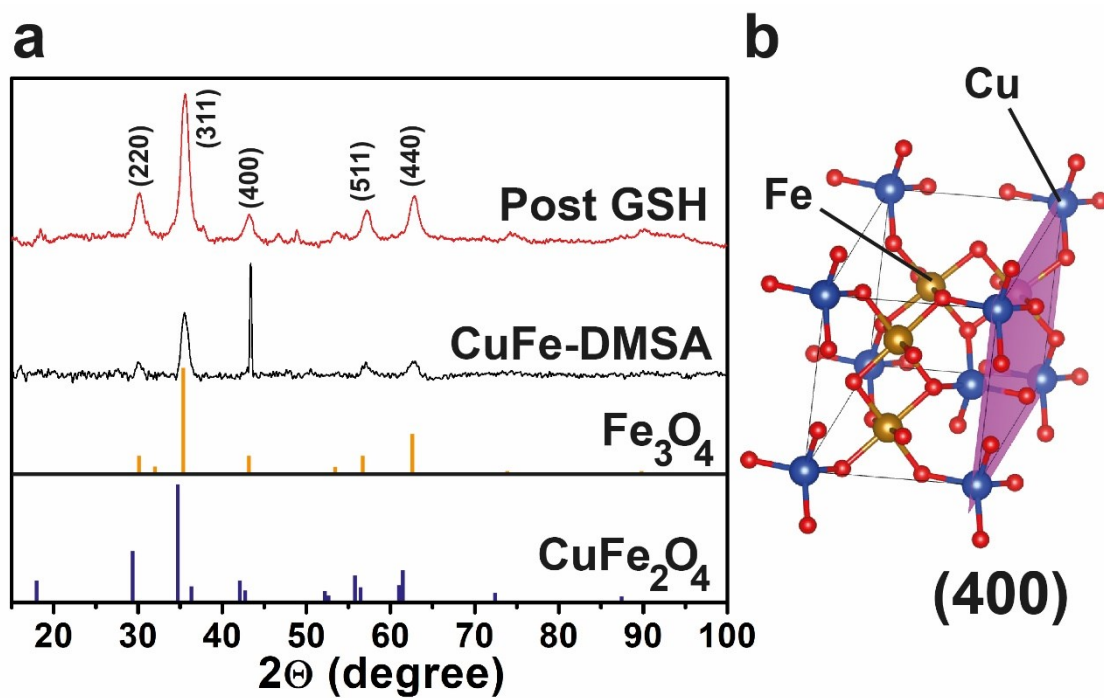


Figure S12. (a) XRD pattern obtained from CuFe-BSA and CuFe-DMSA after reaction with 5 mM of GSH and (b) Cubic structure of CuFe₂O₄ where Fe and Cu occupy octahedral and tetrahedral sites, respectively.

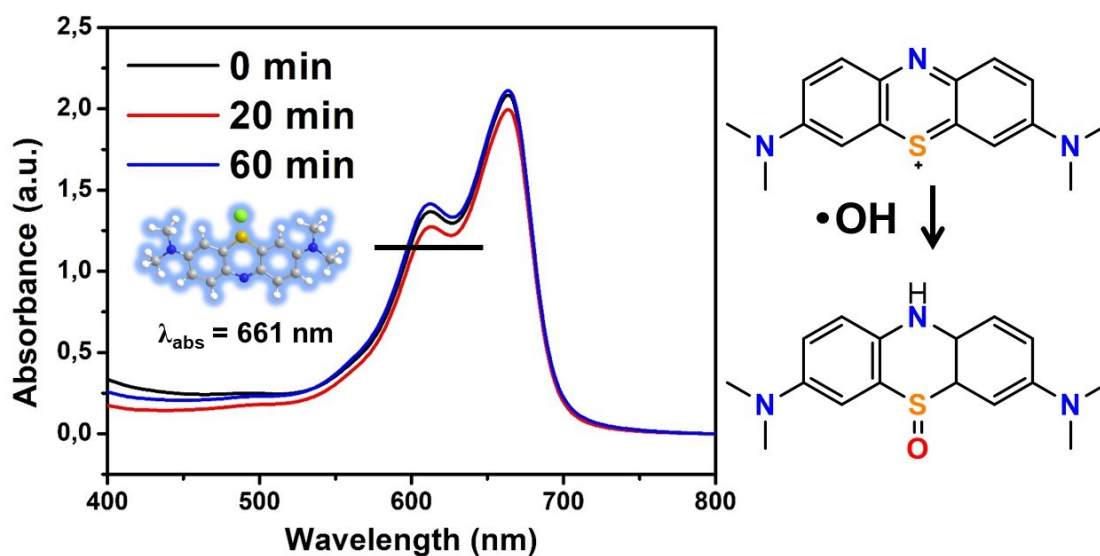


Figure S13. Study of $\cdot\text{OH}$ generation from from reaction of Fe-enriched catalyst ($0.1 \text{ mg}\cdot\text{mL}^{-1}$). UV-vis spectra of Methylene Blue at different times (after CuFe incubation with 5 mM GSH to provoke Cu release) in the presence of H_2O_2 1 mM ($T = 25 \text{ }^\circ\text{C}$, $\text{pH} = 6.5$ (adjusted with CH_3COO^- 0.05 M)).

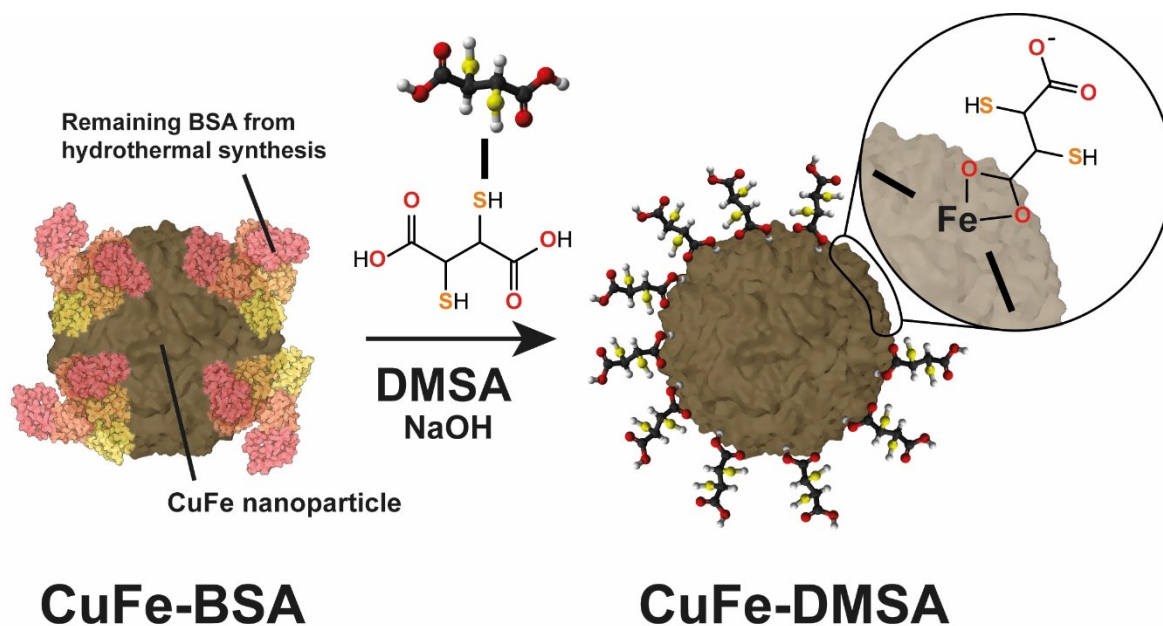


Figure S14. CuFe-DMSA synthesis route. A ligand exchange process is applied to as-synthesized CuFe-BSA nanoparticles to promote the replacement of BSA remaining from the hydrothermal synthesis by DMSA. An alkaline medium is necessary to solubilize DMSA into the aqueous media. Once deprotonated, carboxyl groups from DMSA are able to bind to Fe^{III} sites in the nanoparticle to enhance the dispersion of the nanoparticles in aqueous media.

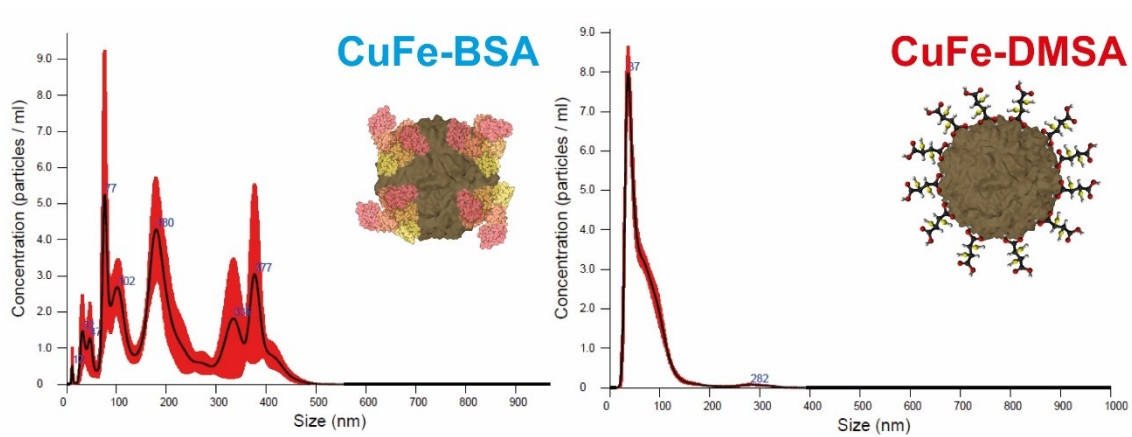


Figure S15. Nanoparticle Tracking Analysis (NTA) of CuFe before (BSA) and after DMSA functionalization, showing the effectiveness of DMSA functionalization to disperse the nanoparticles in aqueous media.

Table S1. Elemental composition of CuFe surface measured by XPS before exposure to GSH.

| Binding Energy (eV) | | | | |
|---------------------|--------|--------|-------|--------|
| Cu 2p | Fe 2p | O 1s | N 1s | C 1S |
| 932.6 | 710.8 | 530.4 | 400.2 | 285.0 |
| 7.80% | 18.74% | 40.15% | 0.81% | 32.47% |

Table S2. Elemental composition of CuFe surface measured by XPS after exposure to GSH.

| Binding Energy (eV) | | | | |
|---------------------|--------|--------|-------|--------|
| Cu 2p | Fe 2p | O 1s | N 1s | C 1S |
| 932.2 | 711.2 | 530.3 | 400.1 | 285.0 |
| 0.28% | 21.00% | 44.24% | 2.52% | 31.96% |

Table S3. XPS quantification of the different Fe and Cu species present on the catalyst surface before exposure to GSH.

| Fe ²⁺ | | Fe ³⁺ | |
|------------------|-------|------------------|-------|
| 2p3/2 | S.O | 2p3/2 | S.O |
| 710.6 | 714.0 | 712.1 | 718.4 |
| 40% | - | 60% | - |

| Cu ^{0/+} | | Cu ²⁺ | |
|-------------------|-------|------------------|-------|
| 2p3/2 | 2p3/2 | S.O.1 | S.O.2 |
| 932.6 | 934.3 | 941.2 | 944.2 |
| 17% | 83% | - | - |

Table S4. XPS quantification of the different Fe and Cu species present on the catalyst surface after exposure to GSH.

| Fe ²⁺ | | Fe ³⁺ | |
|------------------|-------|------------------|-------|
| 2p3/2 | S.O | 2p3/2 | S.O |
| 710.9 | 713.7 | 711.0 | 718.6 |
| 28.5% | - | 71.5% | - |

| Cu ^{0/+} | | Cu ²⁺ | |
|-------------------|-------|------------------|-------|
| 2p3/2 | 2p3/2 | S.O.1 | S.O.2 |
| 932.7 | 934.5 | 941.2 | 943.7 |
| 59% | 41 % | - | - |

Table S5. GSH standards composition employed to analyse GSH-catalytic experiments.

| [GSH] (ppm) | V _{GSH} 100 ppm (μL) | V _{DTNB} 1 mM (μL) | V _{TRIS} 0.01 M (μL) |
|-------------|-------------------------------|-----------------------------|-------------------------------|
| 2.5 | 25 | 100 | 875 |
| 5.0 | 50 | 100 | 850 |
| 10 | 100 | 100 | 800 |
| 20 | 200 | 100 | 700 |
| 40 | 400 | 100 | 500 |

S12. References

- 1 Liu, Y. *et al.* All-in-One Theranostic Nanoagent with Enhanced Reactive Oxygen Species Generation and Modulating Tumor Microenvironment Ability for Effective Tumor Eradication. *ACS Nano* **12**, 4886-4893, doi:10.1021/acsnano.8b01893 (2018).
- 2 Zhang, J. *et al.* Copper ferrite heterojunction coatings empower polyetheretherketone implant with multi-modal bactericidal functions and boosted osteogenicity through synergistic photo/Fenton-therapy. *Chemical Engineering Journal* **422**, 130094, doi:<https://doi.org/10.1016/j.cej.2021.130094> (2021).
- 3 Hai, C. *et al.* Roles of ethylene glycol solvent and polymers in preparing uniformly distributed MgO nanoparticles. *Journal of Asian Ceramic Societies* **5**, 176-182, doi:10.1016/j.jascer.2017.04.004 (2017).
- 4 Behzadi, S. *et al.* Cellular uptake of nanoparticles: journey inside the cell. *Chemical Society Reviews* **46**, 4218-4244, doi:10.1039/C6CS00636A (2017).
- 5 Miguel-Sancho, N. *et al.* Development of Stable, Water-Dispersible, and Biofunctionalizable Superparamagnetic Iron Oxide Nanoparticles. *Chemistry of Materials* **23**, 2795-2802, doi:10.1021/cm1036452 (2011).